12-2013

A Viscous Flow Analog to Prandtl's Optimized Lifting Line Theory Utilizing Rotating Biquadratic Bodies of Revolution

Mark Nathaniel Callender
University of Tennessee - Knoxville, mcallend@utk.edu

To the Graduate Council:

I am submitting herewith a dissertation written by Mark Nathaniel Callender entitled "A Viscous Flow Analog to Prandtl's Optimized Lifting Line Theory Utilizing Rotating Biquadratic Bodies of Revolution." I have examined the final electronic copy of this dissertation for form and content and recommend that it be accepted in partial fulfillment of the requirements for the degree of Doctor of Philosophy, with a major in Engineering Science.

Trevor Moeller, Major Professor

We have read this dissertation and recommend its acceptance:

Peter Solies, Gary Flandro, Lloyd Davis

Accepted for the Council:

Carolyn R. Hodges

Vice Provost and Dean of the Graduate School

(Original signatures are on file with official student records.)

A Viscous Flow Analog to Prandtl's Optimized Lifting Line Theory Utilizing Rotating Biquadratic Bodies of Revolution

A Dissertation Presented for the
Doctor of Philosophy
Degree
The University of Tennessee, Knoxville

Mark Nathaniel Callender
December 2013

Dedication

This dissertation is dedicated to my wife, Sarah, my children, Elijah, Ian, and Elizabeth, and my Lord, Jesus.

Acknowledgements

I would like to express my appreciation to my committee: Trevor Moeller, Peter Solies, Gary Flandro, and Lloyd Davis. They supplied greatly appreciated encouragement and support throughout the process. Many thanks go to Joel Davenport, Jonathan Kolwyck, and Gary Payne for their efforts in building, calibrating, and running the test equipment and water tunnel. Their skill and dedication to moving this project to completion were invaluable. I would also like to thank the University for funding the construction of the experimental test equipment.

Abstract

Prandtl's lifting line theory expanded the Kutta-Joukowski theorem to calculate the lift and induced drag of finite wings. The circulation distribution about a real wing was represented by a superposition of infinitesimal vortex filaments. From this theory, the optimum distribution of circulation was determined to be elliptical. A consequence of this theory led to the prediction that the elliptical chord distribution on a real fixed wing would provide the elliptical circulation distribution. The author applied the same line of reasoning to lift-producing rotating cylinders in order to determine the cylindrical geometry that would theoretically produce an elliptical circulation distribution. The resulting geometry was the biquadratic body of revolution (BBOR). Water tunnel testing was conducted to compare force coefficients and ratios between a lifting arrangement incorporating BBORs and a lifting arrangement incorporating a more traditional cylindrical arrangement, the constant diameter circular cylinder (CDCC). As directed by the Navier-Stokes equation, testing was conducted at low Re, $10^2[100] \leq Re \leq 10^4[10{,}000]$, where viscous effects would become more pronounced. Results showed the BBOR arrangement to produce the highest lift to drag ratio within specific ranges of α [alpha], surface velocity to free stream velocity. Lift coefficients were shown to increase with α [alpha] and approach values an order of magnitude larger than known fixed wing lift coefficients at low Re.

Table of Contents

List of Figures

List of Symbols

a	Distance from strain gage to bearing joint
AR	Aspect ratio
b	Cylinder/bound vortex span, distance between bearing joints
c	Vertical distance from bottom bearing joint to applied force
C	Closed path
C_D	Drag coefficient
C_{D_α}	Drag curve slope
C_L	Lift coefficient
C_{L_α}	Lift curve slope
$C_{L_{max}}$	Maximum lift coefficient
d	Longitudinal distance from vertical connecting bar to applied force
D	Drag
D_i	Induced drag
e	Span efficiency factor
E	Prolate spheroid aspect ratio
F	Force applied to the drag balance bar, resultant force on model
l	Length along a vortex filament, characteristic length
L	Lift
L'	Lift per unit span
L/D	Lift to drag ratio
$(L/D)_{max}$	Maximum lift to drag ratio
M_D	Moment on the vertical balance bar
M_L	Moment on the horizontal balance bar
p	Pressure
p^*	Nondimensional pressure
r	Radial position
r_{avg}	Average cylinder radius
r_0	Radius at the midspan
$\bar{r}$	Prolate spheroid average radius
R	Radius of surface streamline
Re	Reynolds number
s	Distance along a path
S	Planform area
t	Time
t^*	Nondimensional time
V	Velocity
V_{local}	Velocity at the bound vortex
V_r	Velocity in the r-axis in cylindrical coordinates
V_θ	Velocity in the θ-axis in cylindrical coordinates
V_∞	Free stream velocity
V^*	Nondimensional velocity

w	Downwash velocity
x	Flow direction
y	Spanwise axis
z	Vertical axis
α	Ratio of surface speed to the free stream velocity
Γ	Circulation
Γ_0	Circulation at the midspan
Δ_e	Creeping flow cylinder function
θ	Angular position
κ	Doublet strength
Λ	Source strength
μ	Dynamic viscosity
μ^*	Nondimensional dynamic viscosity
ρ	Density
ρ_∞	Free stream density
ρ^*	Nondimensional density
χ	Creeping flow cylinder function
ψ	Stream function, creeping flow cylinder function
ω	Angular velocity
∇	Gradient operator
∇^*	Nondimensional gradient operator

Chapter 1

Introduction and Background

The study of fluid flow is segmented by the effects of viscosity and compressibility. Although all fluids are in actuality viscous and compressible, fluids in certain conditions experience minimal effects of one or both. For example liquids show little volume change with the application of pressure and are therefore deemed incompressible for practical purposes. By contrast gasses show significantly more volume change with the application of pressure and are therefore considered compressible; however, gas dynamic interactions that occur at speeds sufficiently lower than the speed of pressure transmission in the gas can be accurately modeled without the effects of compressibility (Abbott & von Doenhoff, 1959). All fluids, with the exception of superfluids, experience the effects of viscosity. Following Prandtl's discovery and description of the boundary layer, fluid flow was separated into two regions: the boundary layer where viscous effects predominate, and the flow outside of the boundary layer where the effects of viscosity are negligible (Abbott & von Doenhoff, 1959). Derivations of the governing equations of fluid flow may be simplified by the exclusion of viscosity. Conclusions drawn from the simplified equations may prove highly beneficial for inviscid flow, e.g. outside of the boundary layer, yet their applicability can naturally be limited in viscous regions, e.g. the zero drag result known as d'Alembert's paradox. This research points to an application of the results of an inviscid analysis, primarily Prandlt's lifting line theory, to the optimization of a viscous phenomenon, i.e. the Robins-Magnus effect. The basic theories for both are here presented.

Circulation Theory

Kutta-Joukowski theorem. The definition of the aerodynamic tool known as circulation (Γ) is mathematically represented by Equation 1.

$$\Gamma = -\oint_C \boldsymbol{V} \cdot \boldsymbol{ds} \tag{1}$$

The interpretation of Equation 1 is aided by Figure 1 and proceeds as follows. The scalar product of velocity (V), in a given velocity field, is taken with ds, representing an infinitesimal distance along a closed curve C. The sum of all such products around C is known as circulation. The significance of circulation is that for a two dimensional (infinite) body immersed in a velocity field about which the circulation is finite $(\Gamma < \infty, \Gamma \neq 0)$, the theorem of Kutta-Joukowski states that a force will be produced on the body perpendicular to the oncoming flow (Anderson, 2007). The simplified Kutta-Joukowski theorem is given by Equation 2.

$$L' = \rho_\infty V_\infty \Gamma \tag{2}$$

The force experienced by the body is designated L', since aero/hydrodynamic lift (L) is also by definition perpendicular to the oncoming flow (V_∞). The force being per unit span is represented by the prime (L').

Inviscid incompressible flow with circulation. Velocity fields with circulation can be represented mathematically; however, the velocity field must correspond to reality in order to have physical significance. The description of one such field follows. In order to provide an Eulerian description of flow, the velocity must be presented as a function of its position. The stream function (ψ) provides such a description. Differentiating a stream function produces a function that defines particle velocities at every point in space. The path of a particle is known as a streamline (for flow with no time variation, i.e., steady flow (Karamcheti, 1966)). Two conditions must be met prior to using a stream function. The flow must be incompressible everywhere. This condition is presented in Equation 3.

$$\nabla \cdot V = 0 \tag{3}$$

In addition the flow must be irrotational everywhere, as presented by Equation 4.

$$\nabla \times V = 0 \tag{4}$$

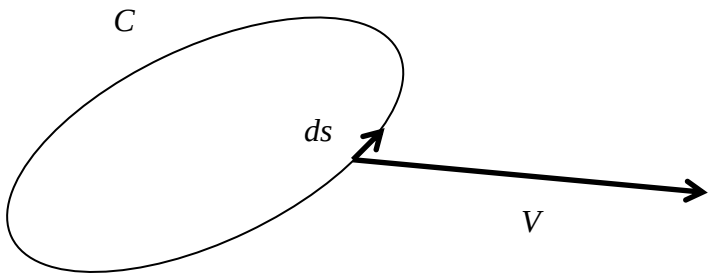

Figure 1. Circulation. A closed curve C with an elemental length ds in a velocity field having velocity V at ds.

Given the two conditions, the stream function for a velocity field is a solution to Laplace's equation as shown by Equation 5.

$$\nabla^2\psi = 0 \tag{5}$$

A solution to Laplace's equation is linear and therefore may be superposed to form other solutions (Anderson, 2007). Velocities in polar coordinates may be derived from stream functions as shown in Equation 6.

$$V_r = \frac{1}{r}\frac{\partial\psi}{\partial\theta} \tag{6.a}$$

$$V_\theta = -\frac{1}{r}\frac{\partial\psi}{\partial r} \tag{6.b}$$

Several fundamental stream functions and associated velocities in cylindrical coordinates are as follows. The first and most basic is that of the uniform stream as given by Equation 7 with velocities given by Equation 8.

$$\psi = V_\infty r sin\theta \tag{7}$$

$$V_r = V_\infty cos\theta \tag{8.a}$$

$$V_\theta = -V_\infty sin\theta \tag{8.b}$$

The next stream function is that of a source as given by Equation 9 (Anderson, 2007).

$$\psi = \frac{\Lambda}{2\pi}\theta \tag{9}$$

The velocity produced by a source (V_r) emanates radially outward from a point as shown in Figure 2 with decreasing magnitude as given by Equation 10 (Anderson, 2007).

$$V_r = \frac{\Lambda}{2\pi r} \tag{10}$$

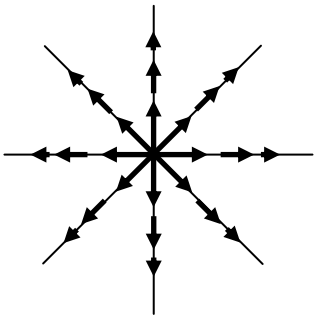

Figure 2. Source Flow. The direction and magnitude of velocities are shown to radiate outward and decrease with radial distance from the source.

The strength of the source is represented by Λ. The next stream function is that of a sink as given by Equation 11 (Anderson, 2007).

$$\psi = -\frac{\Lambda}{2\pi}\theta \tag{11}$$

The velocity (V_r) induced by a sink gravitates radially inward toward a point as shown in Figure 3 with increasing magnitude as given by Equation 12 (Anderson, 2007).

$$V_r = -\frac{\Lambda}{2\pi r} \tag{12}$$

As is evidenced by Equations 11 and 12 and seen in Figure 3, a sink is the opposite of a source. Since both sources and sinks are solutions to Laplace's equation, they may be superposed. The superposition of a source and a sink at the same location is known as a doublet with strength κ, as given by Equation 13, with velocity given by Equation 14 as shown in Figure 4 (Anderson, 2007).

$$\psi = -\frac{\kappa}{2\pi}\frac{sin\theta}{r} \tag{13}$$

$$V_r = -\frac{\kappa}{2\pi}\frac{cos\theta}{r^2} \tag{14.a}$$

$$V_\theta = \frac{\kappa}{2\pi}\frac{sin\theta}{r^2} \tag{14.b}$$

Flow emanating from the source is drawn back into the sink following circular streamlines. The superposition of a uniform stream and a doublet results in a streamline leading to a point of zero velocity known as a stagnation point. From the stagnation point, semicircular streamlines emanate in opposite directions encircling the doublet and meeting in a second stagnation point on the opposite side from which the leading streamline appears to exit away from the doublet. Further streamlines originating above and below the stagnation streamline continue smoothly above and below the stagnation and semicircular streamlines. This flow is pictured in Figure 5. The semicircular streamlines connecting the two stagnation points form a circle. This mathematical

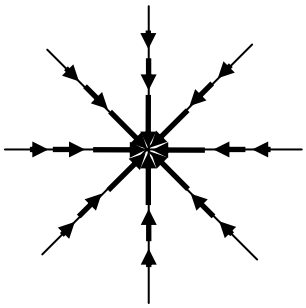

Figure 3. Sink Flow. The direction and magnitude of velocities are shown to gravitate inward and decrease with radial distance from the source.

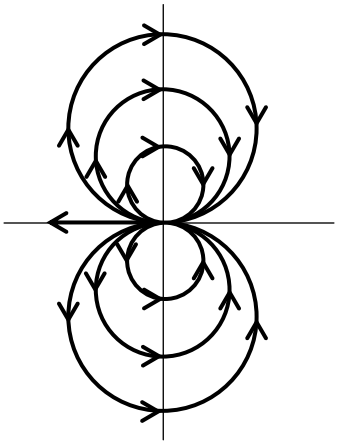

Figure 4. Doublet Flow. The direction and magnitude of velocities follow circular streamlines from the source to the sink. The direction of the doublet is to the left.

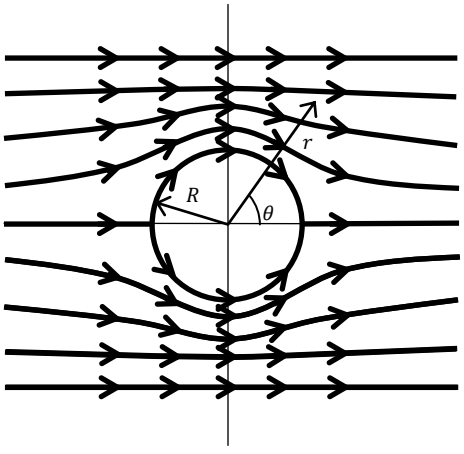

Figure 5. Doublet Flow in a Uniform Stream. Stagnation streamlines can be seen to enter and exit from the circular streamlines while other streamlines pass over and below.

construction represents the incompressible, inviscid flow around an infinite cylinder. The velocity for this flow is calculated via Equation 15.

$$V_r = \left(1 - \frac{R^2}{r^2}\right) V_\infty cos\theta \tag{15.a}$$

$$V_\theta = -\left(1 + \frac{R^2}{r^2}\right) V_\infty sin\theta \tag{15.b}$$

Radial distance from the center of the cylinder is represented by r as distinguished from the cylinder's radius represented by R. It should be noted that the flow is symmetric about the central streamlines leading into and away from the stagnation points. The magnitudes of the flow's velocities about an axis passing through the doublet's center and normal to its direction are also symmetric. Calculation and integration of pressure along the circular streamlines (or surface of the cylinder) yields zero resultant force. The difference between this result and the reality that a real cylinder in a uniform stream would indeed experience drag is known as d'Alembert's paradox (Pope, 2009). The resolution of d'Alembert's paradox is found by the inclusion of friction, which is absent from the stream function analysis but necessarily involved in real flows. Real flows will be discussed following further discussion of inviscid flows. The next basic inviscid flow is the vortex.

Vortex flows have concentric circular streamlines surrounding the vortex core as represented by the stream function and velocity equation, given respectively by Equations 16 and 17, and as shown in Figure 6.

$$\psi = \frac{\Gamma}{2\pi} lnr \tag{16}$$

$$V_\theta = -\frac{\Gamma}{2\pi r} \tag{17}$$

Here Γ is known as the vortex strength (Anderson, 2007), which is synonymous with circulation as given by Equation 1, and is a constant for the vortex flow although V_θ decreases as the inverse of distance from the vortex core. Superposing a vortex flow with

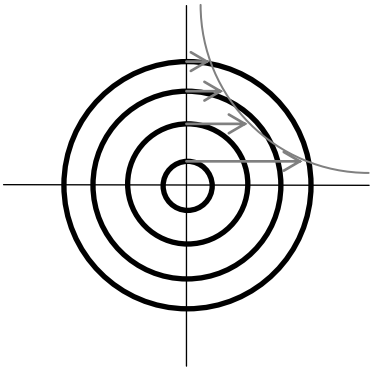

Figure 6. Vortex Flow. Concurrent circular streamlines surround the vortex core. Velocity decreases inversely with distance from the core.

the doublet and uniform stream alters the streamlines as shown in Figure 7. In this Figure, two circular streamlines emanate from a stagnation point and come together at a second stagnation point; however, the leading and exiting streamlines are no longer collinear nor straight, and the stagnation points have moved closer to one another in the flow at the surface of the cylinder. In the case shown, the upper circular streamline has lengthened by the same amount that the lower circular streamline has shortened, thereby bringing the stagnation points closer together. This flow, as is the superposition of the doublet and uniform stream, is symmetric about an axis passing through the center of the doublet and normal to the uniform free stream; however, it is asymmetric about an axis passing through the center of the doublet, which is parallel to the uniform stream. When calculating pressure along the circular streamlines, the symmetry about the vertical axis yields no drag (as with the case of the doublet in the uniform stream); however, the asymmetry about the horizontal axis results in a net pressure and hence a lift force normal to the uniform stream. In addition to the process of pressure integration along the circular streamlines, the value of lift can also be calculated via Equation 2 given the value of Γ for the vortex flow. As with all of the flows mentioned heretofore, this flow is inviscid. It is this final basic flow and the lift force that results that forms the foundation of this work. As a closing note on inviscid, incompressible 2-D flows, streamlines exist within the circular streamlines of Figures 5 and 7; however, the flow of interest lies outside this region. The inner flow is therefore ignored for the mathematical benefit of excluding singularities at $r = 0$ for the doublet and vortex flows, as well as for the physical reason that solid bodies will be considered to occupy this position.

Robins-Magnus Effect

The superposition of basic inviscid flows (uniform stream, doublet, and vortex) results in what appears to be a lifting cylinder. The cylinder itself is created by the doublet and uniform stream. Lift on the cylinder is a result of the addition of circulatory vortex flow, non-zero Γ. Rotation of a real cylinder in inviscid flow has no way to impart circulation to the surrounding fluid; inviscid flow with circulation is mathematical, not

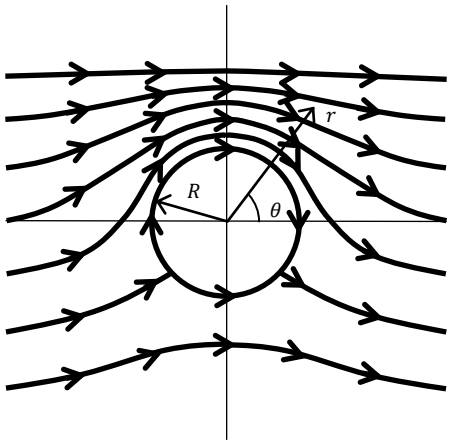

Figure 7. Vortex Flow with a Doublet in a Uniform Stream. Streamlines are drawn over the circular streamlines causing asymmetry about the horizontal axis passing through the vortex/doublet core.

real. However, rotation of a cylinder in viscous (real) flow does impart circulation to the surrounding fluid via friction. Velocity is imparted to the adjacent fluid through skin friction (the no-slip boundary condition), and the fluid's viscosity transmits velocity to adjoining layers away from the surface similar to the velocity distribution shown in Figure 6 for inviscid vortex flow. The addition of a freestream velocity to a rotating cylinder will result in a lifting force analogous to the force on an apparent cylinder calculated for inviscid flow. This flow is shown by the visualization in Figure 8. The production of a lift force by a real rotating cylinder in real flow is known as the Robins-Magnus effect (Sengupta & Talla, 2012).

Much analytical, experimental, and numerical effort has been devoted to the Robins-Magnus effect. Moore (1957) presented a first order analytical approach to the viscous flow about an infinite rotating cylinder that produced results identical to the Kutta-Joukowski theorem. Prandtl (1926) presented a theoretical maximum lift coefficient for infinite rotating cylinders, $C_{L_{max}} = 4\pi$, beyond which increases in the ratio of rotational speed to forward speed, α, would no longer increase the lift coefficient. This is reached when the fore and aft stagnation points meet on one side of the cylinder. Reid's (1924) experimental results showed lift coefficients for rotating cylinders an order of magnitude greater than typical airfoils $\left(C_L = \mathcal{O}(10)\right)$ with an $(L/D)_{max}$ value of approximately 7.8 for $Re = 4 \times 10^4$ and $\alpha \sim 2.5$. Ou (1991), Ou & Burns (1991), and Burns & Ou (1993) presented numerical results for unsteady flow over rotating cylinders that showed similar increasing values of C_L and similar L/D to that of Reid; however, Ou and Burns reported a time averaged $C_{L_{max}}$ of approximately 6.25 and $(L/D)_{max}$ of approximately 4.6 for $Re = 200$ and $\alpha \sim 2.38$ (instantaneous values were higher). At similar rotation rates, Karabelas *et al*. (2011) presented numerical results of $(L/D)_{max}$ of approximately 5.3 for $Re = 5 \times 10^5$. Chew, Cheng, & Luo (1995) presented an $(L/D)_{max}$ of 4 and $C_{L_{max}}$ of 9.1 for $Re = 10^3$ and $\alpha = 2$. Beyond strictly force information, Stojkovic, Schon, Breuer, & Durst (2003) numerically discovered the presence of two distinct vortex shedding modes for infinite rotating cylinders for $60 \leq Re \leq 200$. They showed that for $\alpha \lesssim 1.9$ and $4.35 \lesssim \alpha \lesssim 5.45$ vortex shedding

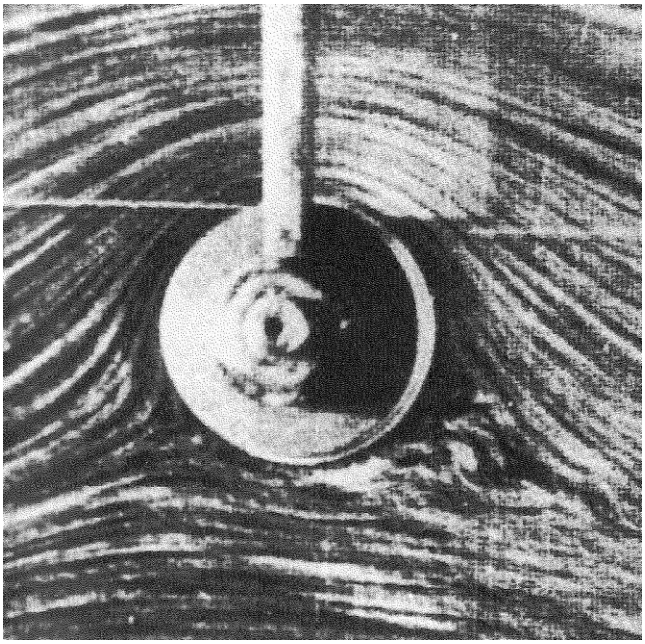

Figure 8. Robins-Magnus Effect. Streamlines around a rotating cylinder exhibit striking similarity to the streamlines for a vortex/double/uniform flow superposition (Prandtl & Tietjens, 1957).

modes existed outside of which the flow exhibited steady behavior (Stojkovic, Schon, Breuer, & Durst, 2003). Stojkovic *et al*. (2003) also observed that within the second shedding mode (for higher α) the average drag coefficient was negative (i.e. thrust was produced), and beyond the second shedding mode the flow field resembled the potential flow solution for a rotating cylinder. Stojkovic, Breur, & Durst (2002) also showed numerically an asymptotic increase in C_L with α towards Prandtl's limit of 4π at $Re = 100$. Many other works have presented similar results (Badr, Coutanceau, Dennis, & Menard (1990); Chen, Ou, & Pearlstein (1993); Kang, Choi, & Lee(1999); Chou (2000); and Lu, Qin, Teng, & Li (2011)). Glauert (1957) presented theoretical values of C_L that far exceeded the maximum presented by Prandtl; however, he presented no Re nor L/D information. Tokumaru & Dimotakis (1993) presented experimental results showing greater lift coefficients than Prandtl's theoretical maximum, possibly due to flow instabilities (Sengupta & Talla, 2012). They presented $C_{L_{max}} \sim 15.4$ for $Re = 3.8 \times 10^3$. Mittal & Kumar (2003) presented numerical results for infinite circular cylinders that also showed C_L values far exceeding Prandtl's theoretical maximum for increasing values of $\left(C_{L_{max}} \sim 27, \alpha = 5, Re = 200\right)$. Padrino & Joseph (2006) numerically verified and extended Mittal & Kumar's results for higher α and $\left(C_{L_{max}} \sim 34, \alpha = 6, Re = 400\right)$. Although numerical results have been presented for finite rotating circular cylinders (Mittal S. , 2004), experimental results have been gathered from essentially two-dimensional circular cylinders given that the models spanned the wind tunnel test section or were capped with end plates or fairings. Table 1 presents a collection of referenced results for rotating cylinders.

Table 1.

Circular Cylinder Results

Researcher(s)	$C_{L_{max}}$	$(L/D)_{max}$	Re	α	Investigation Type
Prandtl	4π	-	-	2	Analytical, 2D
Reid	9.5*	7.8	4×10^4	2.5	Experimental, 2D
Ou & Burns	6.25	4.6	2×10^2	2.38	Numerical, 2D
Karabelas *et al.*	2.3*	4.7	5×10^6	2	Numerical, 2D
Chew, Cheng, &Luo	9.1	4	1×10^3	2	Numerical, 2D
Stojkovic, Breur, & Durst	$2\pi\alpha$	-	1×10^2	≥ 5.5	Numerical, 2D
Tokumaru & Dimotakis	15.4*	-	3.8×10^3	10	Experimental, 2D
Mittal & Kumar	27	-	2×10^2	5	Numerical, 2D
Padrino & Joseph	34	-	4×10^2	6	Numerical, 2D

* This was the highest achieved in testing but no absolute maximum was identified.

Lifting Line Theory

Anderson (2007) explains how Prandtl adapted the Kutta-Joukowski theorem to finite "lifting lines" with bound and trailing vortices. A vortex filament with strength Γ and length b is used to represent a finite wing of the same length as shown in Figure 9. The vortex filament replacing the wing is known as the bound vortex. According to Helmholtz's theorem, a vortex cannot begin or end in a fluid except at a boundary (Karamcheti, 1966); therefore, vortices must continue from the ends of the bound vortex and do so in the direction of the uniform stream as seen in Figure 9. These vortices are known as trailing vortices and are analogous to wingtip vortices trailing behind finite wings. The bound and trailing vortices in combination are referred to as a horseshoe vortex. Although not necessarily relevant to the discussion at hand, the trailing vortices must also abide by Helmhotz's theorem. In doing so, they are themselves connected by a vortex filament known as the starting vortex that closes the vortex filaments leaving no open ends. According the law of Biot-Savart given by Equation 18, velocities are induced everywhere in the flow by the bound and trailing vortices (Anderson, 2007).

$$dV = \frac{\Gamma}{4\pi}\frac{\boldsymbol{dl}\times\boldsymbol{r}}{|\boldsymbol{r}|^3} \tag{18}$$

Therefore each segment, dl, of a trailing vortex induces a velocity, dV, at a given location along the bound vortex a given distance, r, from the segment. The influence of the entirety of the trailing vortices upon the bound vortex produces a downward velocity along the bound vortex known as downwash, $w(y)$, distributed along its length. The downwash velocity causes the local relative wind, V_{local}, at the bound vortex to be slightly different than the uniform free stream, V_∞. The local lift force, calculated via Equation 2, is then perpendicular to the local relative wind but tilted back in relation to the uniform stream as shown in Figure 10. Lift is by definition perpendicular to the relative wind (uniform free stream), so the sum of the force components perpendicular to

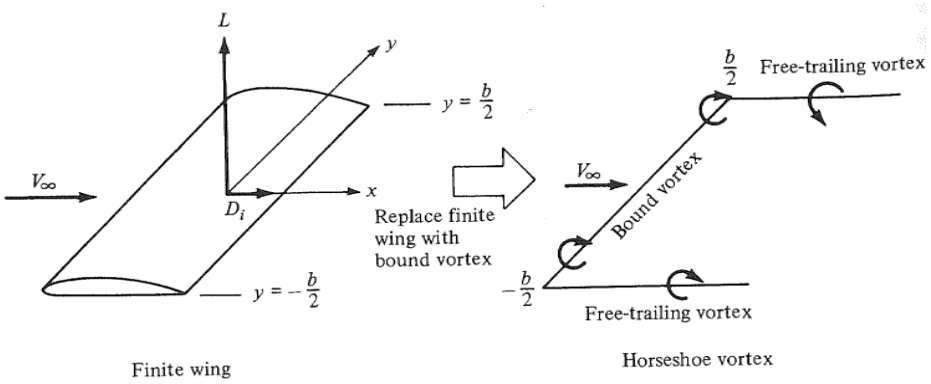

Figure 9. Horeshoe Vortex Representation of a Wing. A Finite wing is replaced by a bound vortex with trailing vortices analogous to those formed at real wingtips (Anderson, 2007).

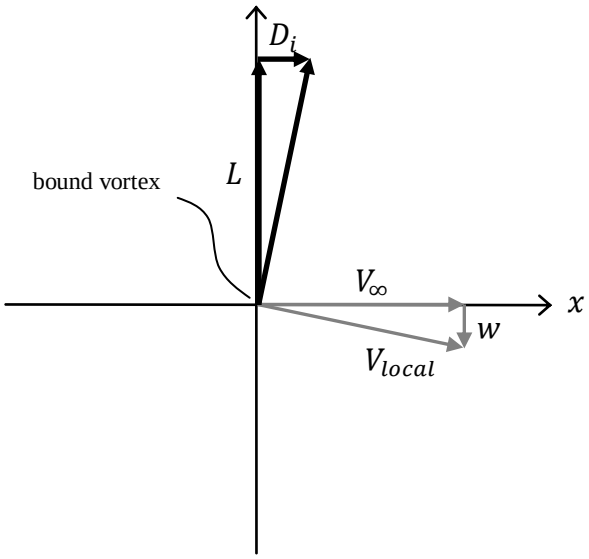

Figure 10. Velocity and Force Effects at the Bound Vortex. The downward component of velocity, *w*, induced by the trailing vortices causes the force at the bound vortex to be tilted in the direction of the uniform stream.

the relative wind is lift, but the sum of the force components parallel to the relative wind is known as induced drag, D_i, as presented in Figure 10.

The system of vortices by which lift and induced drag can be calculated came to be known as Prandtl's lifting line theory. The lifting line theory is the three dimensional extension of the circulation theory by which lift, and now induced drag, for a finite wing, not simply an airfoil, may be calculated using incompressible, inviscid analysis. Lifting line theory goes further in modeling the lift produced by a real finite wing by noting that the lift goes to zero at the wingtips where the pressures on the upper and lower surfaces equalize. This requires a lift and necessarily a circulation distribution, $L(y)$ and $\Gamma(y)$ respectively, which goes to zero at the ends of the bound vortex. Anderson (2007) presents a step by step description of creating such a distribution. To begin with, several horseshoe vortices are superposed with the bound vortex of each being coincident. As with basic two dimensional flows, these vortices are added thus providing a rough circulation distribution as shown in Figure 11. As the number of horseshoe vortices is increased to infinity, the distribution becomes smooth and truly goes to zero at the ends of the combined bound vortex. A continuous sheet of trailing vortices is then shed from the bound vortex as opposed to only two distinct trailing vortices. A continuous circulation distribution is presented in Figure 12. As with the distribution of lift more closely resembling that of a real finite wing, so too a trailing vortex sheet more accurately models the trailing vortices of a real finite wing that does indeed shed vorticity along its length not simply at the wingtips. By the lifting line theory the lift and induced drag of a finite wing in an inviscid, incompressible fluid can be calculated when a circulation distribution ($\Gamma(y)$, with the y axis located along the span) is given. For a fixed wing with known airfoil sections and chord and twist distributions, $\Gamma(y)$ and hence L and D_i can be calculated with knowledge of the lift characteristics of each airfoil section. Conversely for a given $\Gamma(y)$, a wing's chord and/or twist distribution can be determined. A final note: Prandtl's lifting line is formed by vortex filaments having no thickness and by definition has an infinite AR.

Circulation distribution for minimum induced drag. Munk (1921), a student and colleague of Prandtl, utilized the lifting line theory to solve for a particular $\Gamma(y)$ such

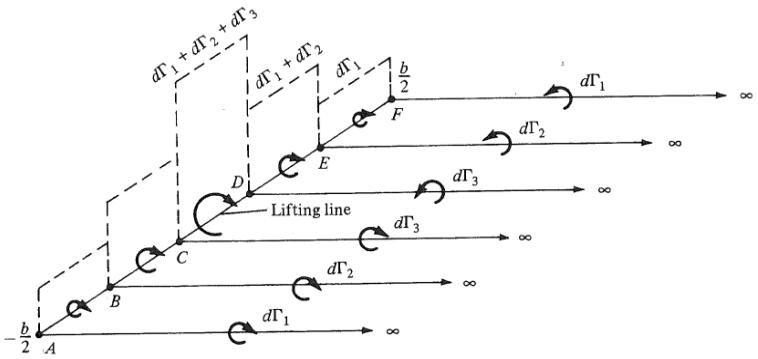

Figure 11. Superposition of Discrete Horseshoe Vortices. Horseshoe vortices are superposed to approximate the distribution of circulation for a finite wing *(Anderson, 2007)*.

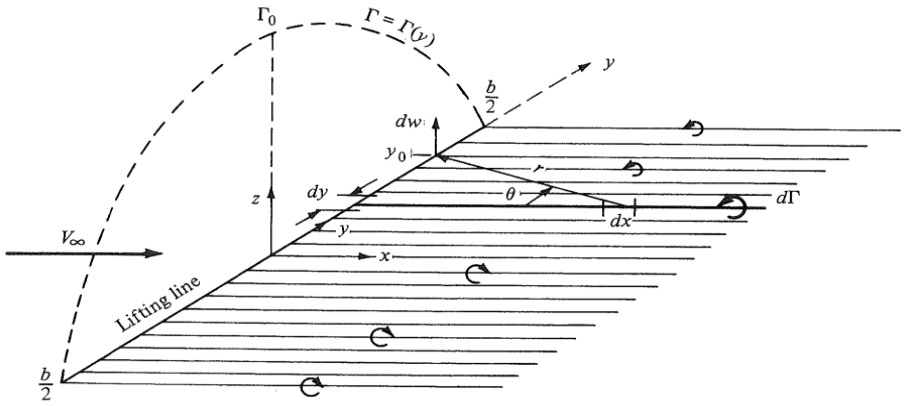

Figure 12. Superposition of Continuous Horseshoe Vortices. The continuous distribution of infinitely many infinitesimal horseshoe vortices represent the actual circulation distribution of a finite wing with circulation decreasing to zero at the wingtips *(Anderson, 2007)*.

that D_i was minimized. The $\Gamma(y)$ that accomplished this is the elliptical distribution, which has the form of Equation 19 and is shown in Figure 13.

$$\Gamma(y) = \Gamma_0 \sqrt{1 - \left(\frac{2y}{b}\right)^2} \tag{19}$$

The span, represented by b, y runs from $-b/2$ to $b/2$, and $\Gamma(0) = \Gamma_0$. An outcome of the elliptical $\Gamma(y)$ is that the calculated chord distribution, $c(y)$, is also elliptical when the wing is untwisted and composed of only one airfoil section (Anderson, 2007). As an aside, continued analysis of the elliptical $\Gamma(y)$ has been made regarding span camber. When a wing has no span camber, the wing's representative lifting line is contained within the x-y plane and is known as planar. When a wing has span camber, the wing's lifting line is no longer confined to the x-y plane and is said to be nonplanar. Dihedral, winglets, endplates, and curved spans lead to the categorization of a wing as nonplanar. Such wings have been investigated by Cone (1962), Kroo (2000), Lundry & Lissaman (1968), Lyapunov (1993), and Mangler (1938). While reductions in D_i are consistently shown for nonplanar wings, Lyapunov(1993) showed that for a planar lifting line with the same total length as a corresponding nonplanar lifting line, the planar lifting line, with an elliptical $\Gamma(y)$, will have lower D_i. It is for this reason that this work is founded on planar wings and hence straight lifting lines.

The current state of the art in lift production by rotating cylinders via the Robins-Magnus Effect considers constant diameter circular cylinders (CDCC). Numerical investigations have presented results for finite CDCCs; however, theoretical and experimental investigations have presented results for 2D cylinders.

The state of the art is expanded by this work as follows: 1) a theoretical optimization of the cylindrical geometry used for lift production via the Robins-Magnus Effect is developed resulting in the biquadratic body of revolution (BBOR), 2) an experimental system to include a force balance and a mechanism for driving rotating cylinders in a water tunnel at low Re is presented, and 3) the results from the comparison of CDCC and BBOR arrangements is presented.

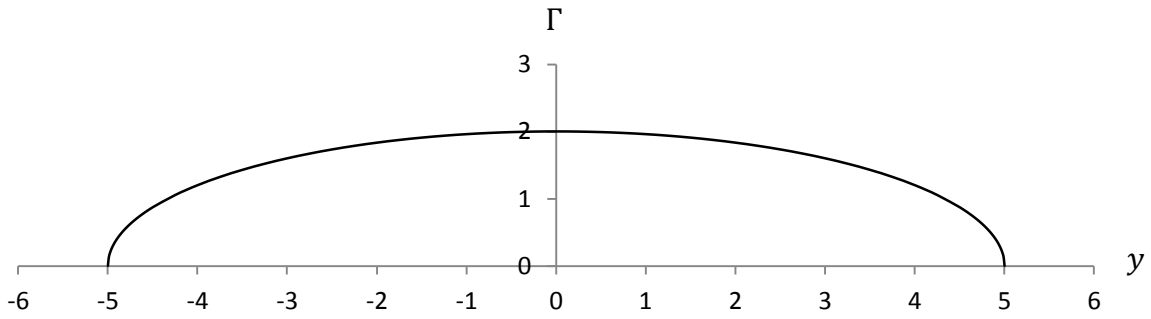

Figure 13. Elliptical Distribution of Circulation.

Chapter 2

Theoretical Development

Biquadratic Body of Revolution

Prandtl's lifting line theory provides a means to calculate lift and induced drag given a bound vortex with a known distribution of circulation, $\Gamma(y)$. The optimized distribution of circulation is elliptical. Given the elliptical circulation distribution, the elliptical chord distribution for a finite fixed wing follows. Therefore lifting line theory is used to design an optimized fixed wing. The Robins-Magnus effect describes lift produced not by fixed wings but by rotating cylinders or bodies. Regardless of whether lift is produced by the effects of camber and angle of attack for fixed wings or by body rotation for rotating cylinders, the value of circulation is central according to circulation theory and by extension to Prandtl's lifting line theory. The author began to analyze the optimization of a rotating body creating lift via the Robins-Magnus Effect by focusing on circulation. The analysis began two dimensionally.

Whereas circulation may be calculated for an airfoil, fixed (nonrotating) airfoils don't have an intuitive connection with the word circulation. An infinite (2-D) rotating cylinder however, does cause the surrounding fluid to "circulate" due to friction at the surface. This "circulation" provided an intuitive connection with the value of circulation determined by Equation 1. According to Equation 1, the value of Γ was independent of the path C; therefore, C may be chosen based upon ease of calculation. The path chosen around a rotating cylinder for this analysis was one adjacent to the cylinder's surface. This choice was driven by knowledge of the fluid's velocity at the surface. The no-slip boundary condition implied that the velocity of the fluid (V_r) at the surface (r) was that of the cylinder's surface based upon the angular velocity (ω) of the cylinder and the cylinder's radius (r) as given by Equation 20.

$$V_r = \omega r \tag{20}$$

This velocity was constant at each point along C thereby simplifying the integral in Equation 1 as shown in Equation 21.

$$\begin{aligned}\Gamma &= -\oint_C \ \omega r ds \\ &= -2\pi\omega r^2\end{aligned} \tag{21}$$

As in inviscid flow where the choice of vortex strength (Γ) set the circulation, in viscous flow, the choice of cylinder radius and angular velocity set Γ according to Equation 21. The analysis to this point had been primarily limited to two dimensional flows. Transition was then made to three dimensional flows. Expansion of circulation theory (2-D) to lifting line theory (3-D) led to circulation distributions, $\Gamma(y)$, specifically the elliptical circulation distribution, and the elliptical chord distribution for finite fixed wings. The analysis next developed a similar outcome for finite rotating cylinders.

The basis for lifting line theory was the vortex filament. The usefulness of the vortex filament was contained in the fact that it produces circulation without vorticity (excluding the $r = 0$ position) and could be superposed upon other vortex filaments to create a desired circulation distribution. Rotating cylinders produce irrotational circulation in an analogous manner via Equation 21; however, distributions of circulation produced in this way would require either variable ω or r. Variable ω was not possible for a solid body, but variable r could easily be achieved. As a first attempt, a shape was chosen, and a corresponding circulation distribution was calculated. The elliptical chord distribution for a fixed wing by intuitive analogy led to selection of an elliptical distribution of radii for a cylinder. The body with such a distribution of radius was known as a prolate spheroid, an example of which is shown in Figure 14. The elliptical distribution of radii for the prolate spheroid is given by Equation 22.

$$r(y) = r_0\sqrt{1 - \left(\frac{2y}{b}\right)^2} \tag{22}$$

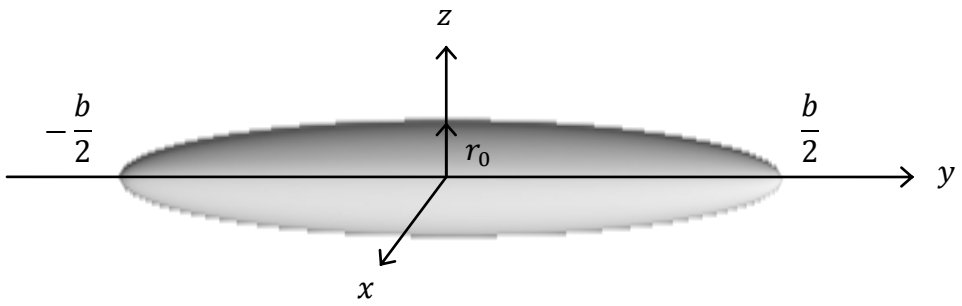

Figure 14. Prolate Spheroid. The prolate spheroid with elliptical distribution of radii.

Here b represents the span of the spheroid, and r_0 represents the radius at midspan $(y = 0)$. The midspan circulation created about a rotating prolate spheroid was calculated by substituting Equation 22 into Equation 1 and integrating as given by Equation 23.

$$\begin{aligned}\Gamma(0) = \Gamma_0 &= -\oint_{C(0)} V(0) \cdot ds(0) \\ &= -\omega r_0 \cdot 2\pi r_0 \\ &= -2\pi\omega {r_0}^2\end{aligned} \tag{23}$$

A similar calculation performed on all spanwise locations, including the substitution of Equation 23, yielded the circulation distribution given in Equation 24 running over the interval $-b/2 \leq y \leq b/2$.

$$\begin{aligned}\Gamma(y) &= -\oint_{C(y)} V(y) \cdot ds(y) \\ &= -2\pi\omega r(y)^2 \\ &= -2\pi\omega {r_0}^2 \left[1 - \left(\frac{2y}{b}\right)^2\right] \\ &= \Gamma_0 \left[1 - \left(\frac{2y}{b}\right)^2\right]\end{aligned} \tag{24}$$

Although the body producing this circulation distribution was a prolate spheroid with an elliptical distribution of radii, the resulting circulation distribution of Equation 24 was parabolic. The elliptical circulation distribution resulting in an elliptical chord distribution for fixed nonrotating airfoils did not prove to be a direct analog for rotating bodies. To arrive at the desired elliptical circulation distribution presented by Equation 19, a different distribution of radii was necessary. A new developmental path was then taken. As opposed to the previous method of choosing a distribution of radii and then solving for the corresponding circulation distribution (of which there were infinite options), the analysis began with the elliptical circulation distribution and proceeded towards the distribution of radii. The elliptical circulation distribution from Equation 18 was first set equal to step two from Equation 24, as shown in Equation 25.

$$\Gamma_0\sqrt{1-\left(\frac{2y}{b}\right)^2} = -2\pi\omega r(y)^2 \tag{25}$$

The distribution of radii in Equation 25 was then isolated, with substitution of Equation 23, and presented in Equation 26.

$$r(y) = r_0\left[1-\left(\frac{2y}{b}\right)^2\right]^{\frac{1}{4}} \tag{26}$$

With rearrangement this took the form of Equation 27.

$$\left(\frac{r(y)}{r_0}\right)^4 + \left(\frac{2y}{b}\right)^2 = 1 \tag{27}$$

Equations 26 and 27 were categorized as biquadratic equations. Since they also represented axisymmetric three dimensional geometries, they were more precisely termed biquadratic bodies of revolution (BBOR). Figure 15 provides an example of such a body. A side-by-side comparison of the prolate spheroid and the BBOR is given in Figure 16. Figure 15 clearly shows the difference in the two geometries especially near the geometries' tips. The BBOR appears blunt compared to the prolate spheroid. By way of analysis, rotation of this body would induce circulatory flow having an elliptical circulation distribution. Theoretical circulation distributions produced by the prolate spheroid and BBOR are shown in Figure 17. Addition of a uniform stream would result in lift via the Robins-Magnus effect analogous to that calculated via Prandtl's lifting line theory. By extension the induced drag, calculated via lifting line theory, would be a minimum for the rotating BBOR as it is for the fixed wing with elliptical chord distribution.

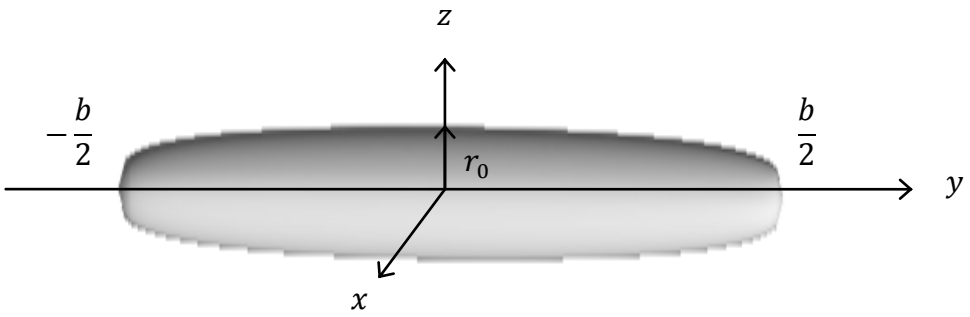

Figure 15. Biquadratic Body of Revolution. The BBOR, when rotated, would produce an elliptical distribution of circulation.

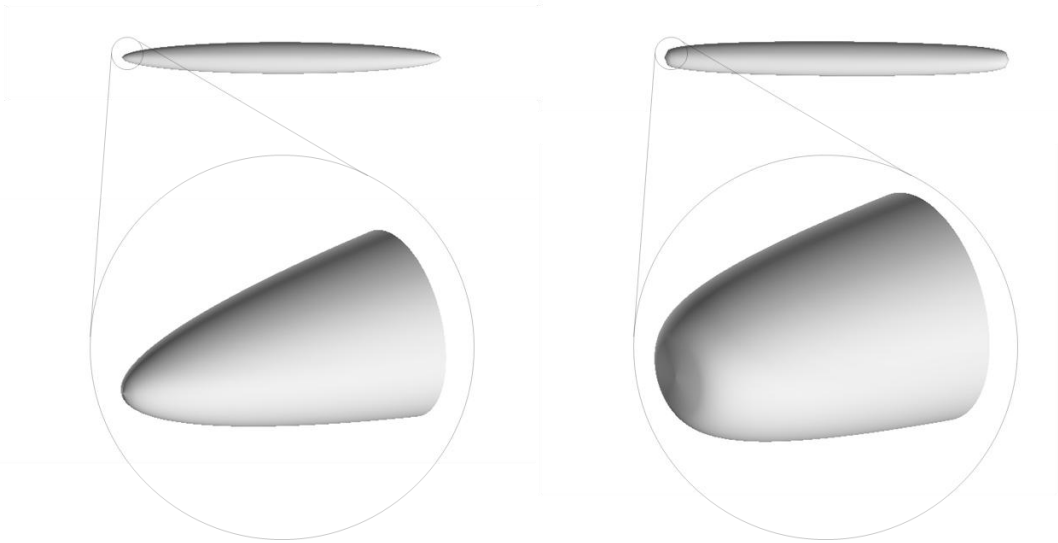

Figure 16. Prolate Spheroid and BBOR Comparison. The differences between the prolate spheroid (left) and the BBOR (right) are most pronounced at the tips. The BBOR is much more blunt at the tips.

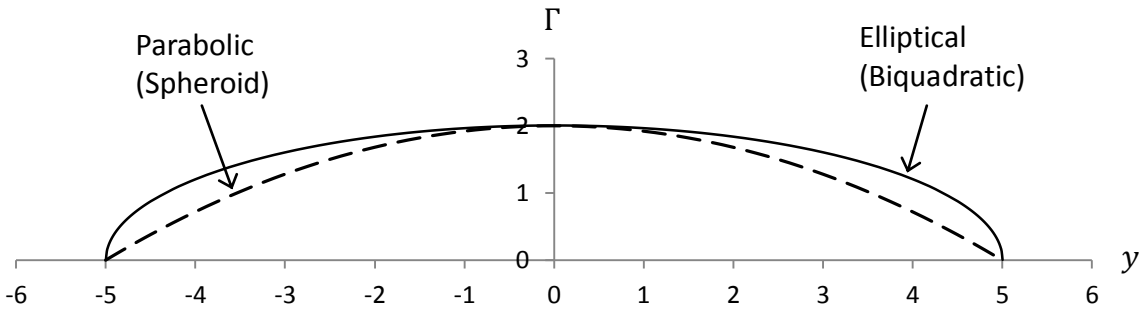

Figure 17. Prolate Spheroid and BBOR Circulation Distributions. The theoretical circulation distributions for each cylindrical geometry (in parenthesis) are presented.

Implications of Navier-Stokes

Considering the inviscid development of Prandtl's lifting line theory, it's applicability to real viscous flows is questionable. For finite fixed wings, the viscous, circulation inducing effects of the wing/fluid interaction are almost entirely contained in a very small region of the flow near the wing's surface known as the boundary layer. Outside of the boundary layer, viscous effects are negligible, and inviscid analysis according to Prandtl's lifting line theory is suitable. Treatment of real fluid flow is described in part by the Navier-Stokes equation, presented nondimensionally (indicated by *) in Equation 28.

$$\rho^* \frac{DV^*}{Dt^*} = -\nabla^* p^* + \frac{1}{Re}\mu^* \nabla^{*2} V^* \tag{28}$$

According to Equation 28, acceleration of the fluid, left side of the equation, is the result of forces of two types: pressure (p) and viscous (μ). The influence of pressure is given by the first term on the right side of Equation 28, while the second term describes the influence of viscosity (i.e. friction). The relative weight of the viscous term is set by the Reynolds number (Re). Reynolds number is a nondimensional dynamic similarity parameter that represents the ratio of viscous to inertial forces given by Equation 29.

$$Re = \frac{\rho V l}{\mu} \tag{29}$$

A characteristic length (l) is often represented by the chord length of an airfoil. High Re flow regimes, according to Equation 28, experience small effects from viscosity. As Re decreases, viscous effects become more influential. The Robins-Magnus effect relies on the viscous interaction between the rotating body and the fluid. It is literally a viscosity-driven circulatory flow and is therefore a highly viscous phenomenon. With this in mind, the viscous term in Equation 28 can be enhanced at low Re. Given that the Robins-Magnus effect experienced by rotating cylinders, specifically BBORs, is a viscosity-driven phenomenon, low Re flow should enhance its effectiveness.

Drag of Nonrotating Cylindrical Bodies

A review of the literature discussing the drag of cylindrical bodies, to include constant diameter circular cylinders (CDCC) and spheroidal and biquadratic bodies of revolution (BBOR), is here presented. Clift *et al*. (1978) presented a general analytical result in creeping flow for the drag coefficient of prolate spheroids whose major axis is normal to the oncoming flow as shown in Equation 30.

$$C_D = \frac{64\bar{r}\left(E^2-1\right)}{\left[\left(2E^2-3\right)ln\left(E+\sqrt{E^2-1}\right)/\sqrt{E^2-1}\right]+E} \tag{30}$$

The author substitutes for Clift *et al. 's* "aspect ratio", E, the wing aspect ratio as given by Equation 31.

$$E = \frac{\pi}{4}AR \tag{31}$$

Clift *et al*. (1978) stated that data, either experimental or numerical for prolate spheroids, are not readily available for higher Re (beyond creeping flow). A review of the literature confirms this statement. Riabouchinsky (1921), Hoerner (1965), and Clift *et al*. (1978) presented analytical and/or experimental results for oblate spheroids without mention of prolate spheroids. Oblate spheroids are spheroids whose axis of rotation (minor axis) is parallel to the oncoming flow. Aoi (1955), Breach (1961) , and Happel & Brenner (1983) presented analytical results for prolate spheroids but only for flow parallel to the major axis. By comparison much theoretical, experimental, and numerical data for circular cylinders was available. Heiss & Coull (1952) presented an expression (with modifications by the author to accommodate for the difference between E and AR) fitted to experimental data for finite cylinders in creeping cross flow shown by Equations 32, 33, 34, and 35.

$$C_D = 6\pi r(3\pi\, AR/8)^{1/3}\Delta_e \tag{32}$$

$$\Delta_e = \frac{1}{\chi\sqrt{\psi}} exp\left[0.576\sqrt{\psi\chi}(\chi - 1)\right] \quad (33)$$

$$\chi = (3/16)^{1/3}\sqrt{\pi}(\pi AR/4)^{-1/6} \quad (34)$$

$$\psi = (18(\pi AR/4)^2)^{1/3}/(\pi AR/2 + 1) \quad (35)$$

Tomotika & Aoi (1950) and Tomotika & Aoi (1951) presented analytical expressions for the drag of infinite circular cylinders at $1 \leq Re \leq 20$. Thom (1933) presents experimental data closely resembling that of Tomotika & Aoi; however, Thom's results covered $3.5 \leq Re \leq 240$. Both Tomotika & Aoi and Thom presented only pressure drag coefficients. Summaries of various experimental results for CDCC drag coefficients as a function of Re were presented in Toussaint (1921), Bairstow, Cave, & Lang (1923), Tritton (1959), Hoerner (1965), Katz & Plotkin (1991), White (2006), Anderson (2007), and many other texts. A representation of cylinder drag coefficients is given in Figure 17. Although many works presented analytical, experimental, and/or numerical results for the drag of circular cylinders, results such as those shown in Figure 17 are primarily two-dimensional. No drag values, experimental or otherwise, were found to exist for BBORs. As can be seen in Figure 18, $Re \sim 3.1 \times 10^3$ presented a local minimum drag coefficient of approximately unity for infinite circular cylinders.

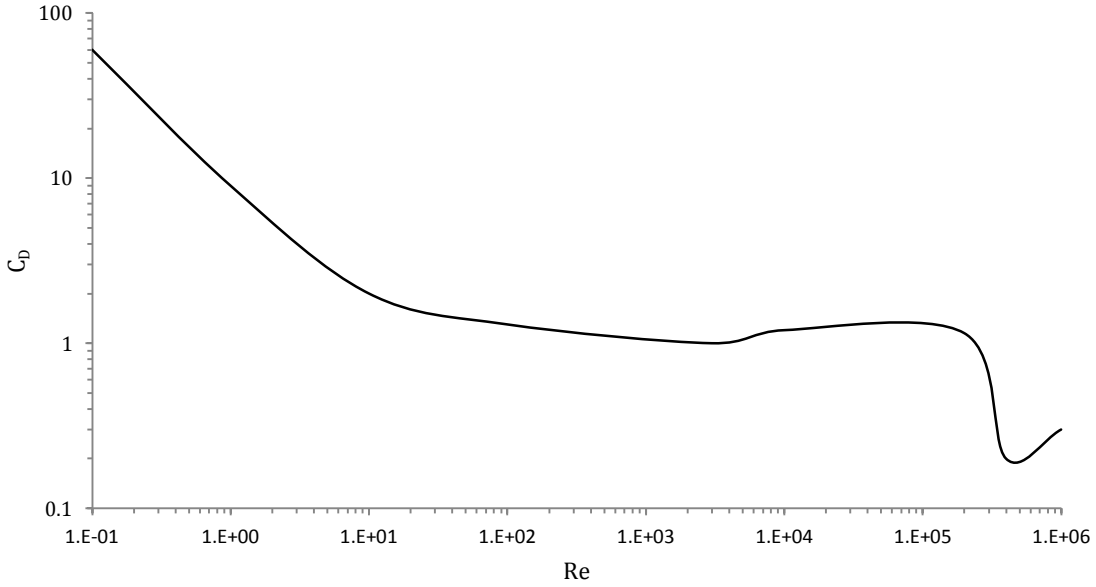

Figure 18. Drag Coefficients. C_D for infinite circular cylinders as a function of Reynolds number, R_e, as recreated from Anderson *(2007)*.

Chapter 3

Experimental Method

Goals

The first goal of the experimental portion of this project was to determine force coefficients, C_L and C_D, and the ratio of these coefficients, C_L/C_D or L/D, for rotating cylinder arrangements at low Re with the cylinder tips free to experience fully 3-D flow. Little to no experimental data existed for the 3-D flow about the constant diameter circular cylinder (CDCC), the geometry typically associated with a cylinder. No data existed for the biquadratic body of revolution (BBOR). The second goal was to compare the coefficients and coefficient ratios of the CDCC and the BBOR arrangements in order to evaluate the prediction that the elliptical circulation distribution theoretically predicted for the BBOR would be realized by providing higher values of C_L/C_D. The target of $Re \sim 3.1 \times 10^3$was chosen due to the low 2-D drag coefficient exhibited by circular cylinders at this Re as shown in Figure 18. This Re was dually chosen due to its central position in the Re range associated with micro air vehicles (MAV). MAVs are unmanned aerial vehicles (UAV) having a maximum dimension of $15\ cm$ that operate in the range $10^2 \leq Re \leq 10^4$. Testing at Re above and below the target was planned in order to determine trends for the model arrangements.

Subjects

CDCC and BBOR. The experiment evaluated two model geometries, the CDCC and the BBOR. The geometries were three dimensional and were meant to rotate about their major/lateral axes (y axis) aligned normal to the oncoming flow. The models were evaluated at equivalent Re. This was accomplished by designing each model to have approximately the same average radius, $r_{avg} = 2.3\ cm$, and adjusting the water tunnel flow speed between model runs accordingly. By maintaining approximately equal r_{avg} and equal cylinder spans, $b = 30.14\ cm$, the models had approximately equal planform areas. Models were constructed from both aluminum and Delrin® acetal resin (Wear- and

Water-Resistant Delrin® Acetal Resin). The Delrin® models were used for testing due to their weight being half that of the aluminum models. The lower weight was an advantage in reducing model vibration while rotating. The aluminum models are shown in Figures 19 and 20. Cylindrical models had historically been tip mounted; however, the 3-D flow induced by and about the models was very important. To capture this, flow about the tips was required to be unaffected.

Model support. With several possible mounting methods considered, including magnetic levitation, the method selected for this experiment was mounting at a central nonrotating fuselage (CNF). The CNF was constructed from ABS plastic in a 3-D printer. The CNF contained an Ondrive PR6-1 sealed worm and wheel gearbox shown in Figure 21, the output shafts of which drove the cylindrical models. A break in the circulation distribution was expected; therefore, the width of the CNF was minimized. A width of 2.2 cm was sufficient for the CNF to contain the necessary components for mechanizing the models' motion. The gearbox was 3.2 cm wide extending outside of the CNF; therefore, the CDCC and BBOR models were counterbored, as shown in Figure 22, to accommodate the width of the gearbox while allowing the models to abut the CNF with minimal gap. Although the entire body did not rotate, the CNF, in addition to providing housing for the mechanism, had the benefit of approximating potential future MAV wing/fuselage interactions. Aft of the gearbox, the CNF supported a Micromotor MMR-0014 sealed pneumatic motor that drove the models. The motor is shown in Figure 23. The motor connected through an Ondrive TLC 13.1824 step-beam coupling to the input shaft of the worm and wheel gearbox. The pneumatic motor had two ports that allowed the rotation to be reversed; however, the research only needed rotation in one direction. One port connected the motor to pressurized shop air, and the other port was connected to an exhaust hose to direct exhaust air away from the models. The air hoses were contained within the CNF from the point of connection to the motor to an exit point above the water level. The upper aft section of the model support containing the air hoses provided a point of connection to the force balance. The CNF is presented in Figure 24. An adapter cap

Figure 19. Aluminum CDCC. The constant diameter circular cylinder model with $r_{avg} = 2.3\ cm$ and a length of $14\ cm$.

Figure 20. Aluminum BBOR. The biquadratic body of revolution model with $r_{avg} = 2.3\ cm$ and a length of $12.7\ cm$ showing the retroreflective tape and set screw location.

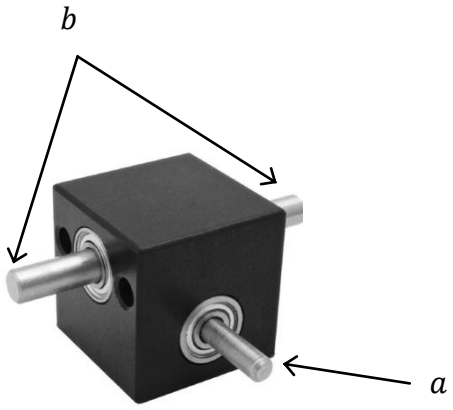

Figure 21. Worm Wheel Gearbox. The gearbox shown with a) the input shaft and b) dual output shafts is slightly smaller than the gearbox used in this project due to the custom inclusion of shaft seals for use in water *(Gearboxes-Small & Miniature)*.

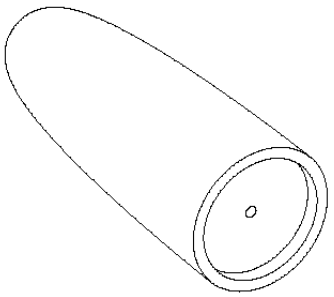

Figure 22. CDCC with Gearbox Counterbore. The width of the gearbox necessitated a counterbore of the models.

Figure 23. Pneumatic Motor. A sealed pneumatic motor was used to drive the gearbox and hence the cylindrical models *(All Air Inc., 2013)*.

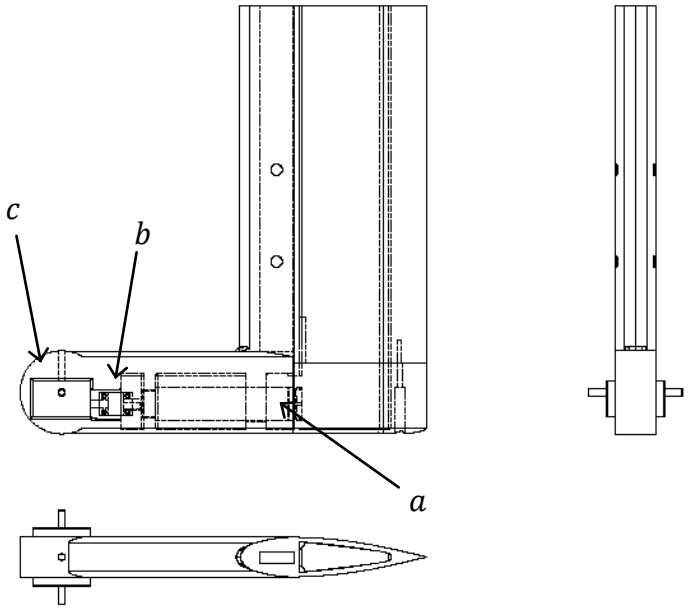

Figure 24. Central Nonrotating Fuselage. The CNF is shown with a) the pneumatic motor, b) the coupling, and c) the gearbox in place.

was also constructed for the CNF to provide a smooth transition for the larger maximum radius, $r_0 = 2.63\ cm$, of the BBOR. The adapter cap is shown in Figure 25.

Design

The experimental design consisted of direct lift and drag force measurement of the rotating cylindrical model arrangements throughout a range of water tunnel flow speeds and rotation speeds. Water flow speed was varied from 0 to $0.46\ m/s$. Model rotation speed was varied from 0 to $900\ rpm$. Water flow speed variation was utilized to achieve a range of Re. For each water flow speed, the cylindrical models' RPM was adjusted to achieve a range of α.

Experimentation at low *Re*. Lissaman (1983) stated that the common difficulties associated with wind tunnel testing (measuring forces of differing magnitudes and different orders of magnitude along different axes, wall boundary effects, turbulence levels, and model shape accuracy) may be amplified in the low Re regime. The difference in magnitude of the forces of lift and drag at high Re can be as much as two orders of magnitude; however, this difference diminishes to single digits for airfoils and rotating cylinders at lower Re ($Re < 10^5$), as shown in Figure 26, making the difference in lift and drag magnitude less drastic in this regime (Lissaman, 1983). The absolute magnitude of the forces also decreases but with different results. A reduction in Re of one order of magnitude, for example, will correspond in up to a two order of magnitude reduction in the forces produced requiring higher sensitivity in the measuring system. Wall boundary effects can be diminished by keeping the model dimensions within 80% of the tunnel section dimensions (Rae & Pope, 1984). Recent work suggested that partially open test sections should be considered to reduce the wall boundary effects when large model deflections were being tested (Worasinchai, Ingram, & Dominy, 2011). Worasinchai, Ingram, & Dominy (2011) show exaggerated values of both C_L and C_D within a closed section tunnel. Large airfoil incidence deflections translate to large flow deflections resulting in increased interaction between the model wake and the tunnel wall(s). Although cylinders would not present geometric differences with incidence changes, flow

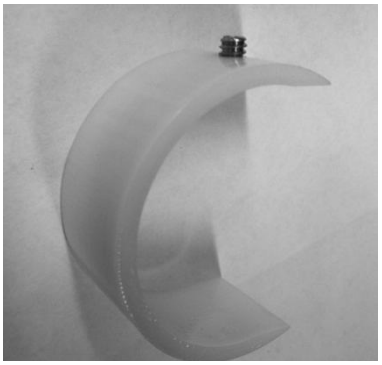

Figure 25. CNF Adapter Cap. The adapter cap with set screw to secure in place when testing BBOR models.

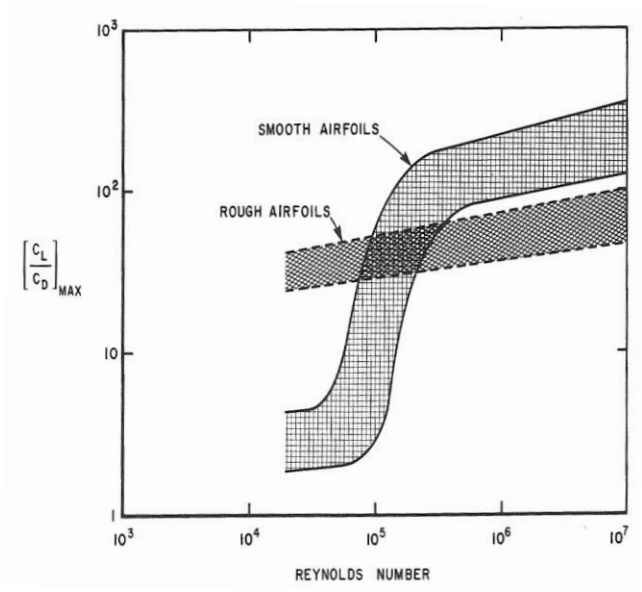

Figure 26. Reynolds number effect on $(L/D)_{max}$ for fixed nonrotating airfoils (Lissaman, 1983).

deflections do increase with α and would therefore require equal consideration, especially along the axis mutually perpendicular to the tunnel flow axis and the cylinder's major axis. Achieving small Re by reduction of model size would assist in keeping models well away from tunnel walls both horizontally and vertically. Turbulence effects may be increasingly pronounced at low Re as turbulent fluctuations become large relative to the lower speeds necessary for low Re operation. Honeycombs and screens are used to reduce the amount of lateral and axial turbulence respectively (Rae & Pope, 1984). Repeatability of results in this regime has been questionable. Carmichael (1981) presented the results from three different testing locations for a common airfoil at $Re = 7 \times 10^4$. The values of $(L/D)_{max}$ reported by two of the facilities were twice as large as the value reported by the third. The former used pressure and wake flow integration while the latter used direct force measurement (Lissaman, 1983). Direct force measurement is arguably preferable; however, as Re decreases, so do the magnitude of the forces. Therefore the sensitivity and resolution of the force balance becomes increasingly important.

Water tunnel. After considering the difficulties involved with low Re testing, the University of Tennessee Space Institute's (UTSI) water tunnel facility was selected as the testing location. UTSI operates an Aerolab water tunnel with a $15" \times 20" \times 60"$ test section capable of water speeds continuously variable from 0 to $3\ ft/s$ (UTSI Research Facilities, 2013). A dye injection system with six dye colors was capable of providing flow visualization (UTSI Research Facilities, 2013). The tunnel is shown in Figure 27. The primary reason for selecting water tunnel testing is the low turbulence level and resistance to turbulent fluctuations achieved in water tunnels. Given the size of the cylindrical models $(r_{avg} \sim 1in)$ and the target Re of approximately 3.1×10^3, a flow speed of around $6\ in/s$ was needed. The water tunnel has an open water boundary at the top of the tunnel. According to Worasinchai, Ingram, & Dominy (2011), the open boundary potentially reduces tunnel boundary effects thereby improving the accuracy of the results.

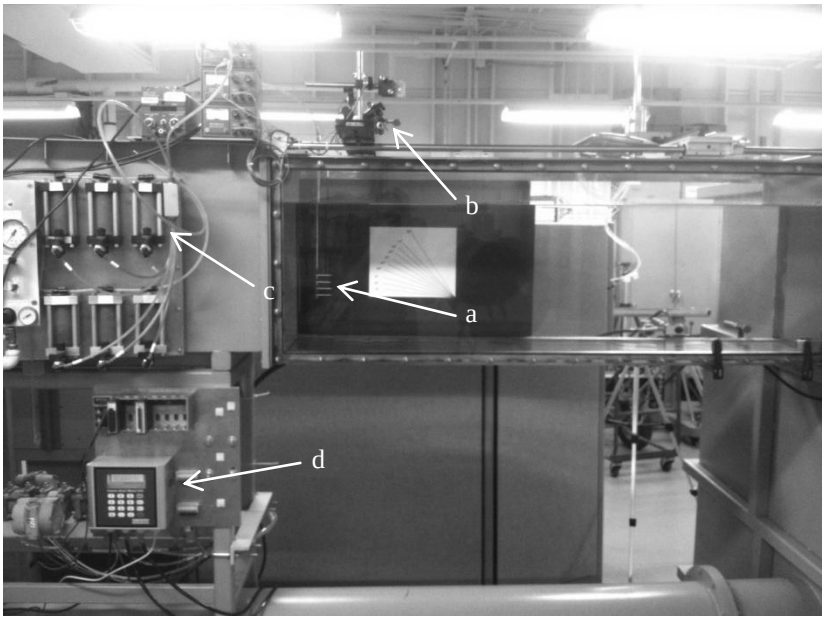

Figure 27. UTSI Water Tunnel. The tunnel test section; dye system to include a) dye ports, b) laser, and c) dye reservoir; and d) flow meter are shown above.

Force balance. No force balance existed for the UTSI water tunnel; therefore, a balance was designed to accommodate this and future experiments. The force balance drawings are presented in the Appendix. For this experiment, the force balance was designed to measure lift and drag forces of the expected magnitude produced by the rotating cylindrical models at Re of approximately 3.1×10^3. The forces were expected to be on the order of 0.1 to $1lb$. The water tunnel force balance is shown in Figure 28. The force balance attached to a vertical rod extending from a rectangular support bar spanning the top of the tunnel sidewalls. The vertical support rod can be seen in Figure 28. The installed balance is shown in Figure 29. The clamp attached to the vertical support rod provided the attachment points for two mutually perpendicular cantilever balance bars. One balance bar was in the horizontal plane, and the other was in the vertical plane. Each balance bar provided two locations, separated by a known distance, to which full Wheatstone bridge strain gage balances were affixed. Deflection of the horizontal bar primarily provided information for lift calculation and will be hereafter referred to as the lift bar, while deflection of the vertical bar primarily provided information for drag calculation and will be hereafter referred to as the drag bar. Two additional bars, one vertical and one horizontal, completed the force balance. These bars were connected to the lift and drag bars and to one another by frictionless C-Flex GD-10 double end bearings. These bearings had torsional spring rates of $.00148\,in-lbs/deg$ offering very low resistance to deflection (C-Flex Bearings Double End Bearing, 2010). This allowed applied forces to transform the original relationship of the balance from a square to a rhombus as the lift and drag bars deflected. The force balance was designed to decouple the lift and drag forces as much as possible. Lift and drag coupling did occur, but the force balance was designed to minimize it. Remaining force coupling was accounted for with proper calibration. Lift forces being typically greater than drag forces required the drag balance to be more sensitive than the lift balance. In order to use the same balance bar design for lift and drag measurements, the vertical connecting bar was longer providing a greater bending moment for the drag bar. This arrangement also allowed the majority of the force balance to remain above the water's surface as seen in Figure 29.

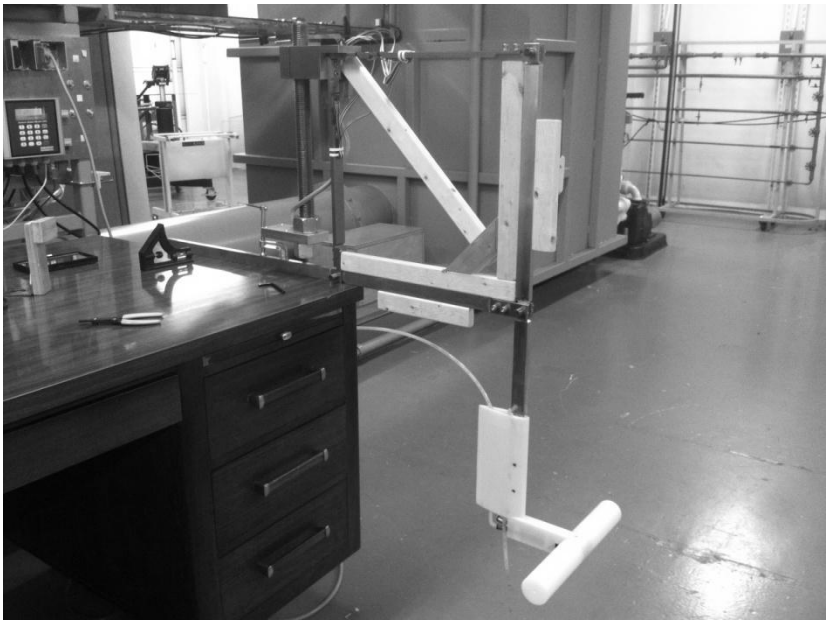

Figure 28. Force Balance with Stabilization Device. The force balance is shown prior to installation with the CNF and CDCCs connected. A wooden stabilization device protects the balance from overstresses during installation, removal, and storage.

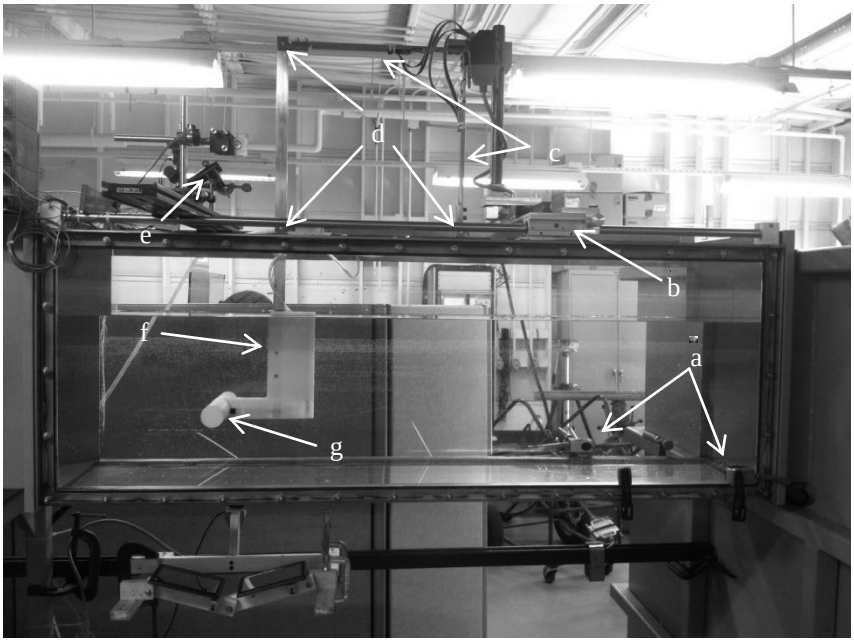

Figure 29. Installed Force Balance. The figure shows the following: a) ultrasonic flow sensors, b) force balance mounting base, c) balance bars, d) C-flex bearing locations, e) laser, f) CNF, and g) mounted CDCC.

Data Collection and Analysis

Data from the custom built force balance was automatically recorded using a National Instruments cDAQ-9188 data acquisition system. The force balance was calibrated by applying known forces in known directions via the calibration system shown in Figure 30. Readings were taken, as basket weight was increased and decreased to account for hysteresis, and then averaged. The calibration device was placed as was shown in Figure 30 as well as aft of the force balance for drag calibration as shown in Figure 31. Uncertainty in basket weight was $\pm$ 0.1 g. The strain gage readings exhibited a large band of linearity with applied force, with nonlinear strain regions at each end. The force calibration curves for the horizontal and vertical balance bars are shown in Figure 32 and Figure 33 respectively.

Water tunnel speed was set and measured with an Innova-Sonic ultrasonic flow meter shown in Figure 29. The tunnel motor was set with the tunnel motor controller, shown in Figure 34. The flow meter was calibrated by post-processing video of dye streams passing behind a measurement device attached to the test section via Equation 36.

$$v = \frac{s_2 - s_1}{t_2 - t_1} \tag{36}$$

Flow speed, the initial and final dye stream positions, and times at those positions, in Equation 36, are represented by v, s_1, s_2, t_1, and t_2 respectively. Uncertainty in the measuring device was $\pm 0.0625\ in$, and uncertainty in the time was $\pm 0.03\ s$. Uncertainty in calculated values was calculated using the basic form of Equation 37 (Taylor, 1982).

$$\delta q = \sqrt{\left(\frac{\partial q}{\partial m}\delta m\right)^2 + \cdots + \left(\frac{\partial q}{\partial n}\delta n\right)^2} \tag{37}$$

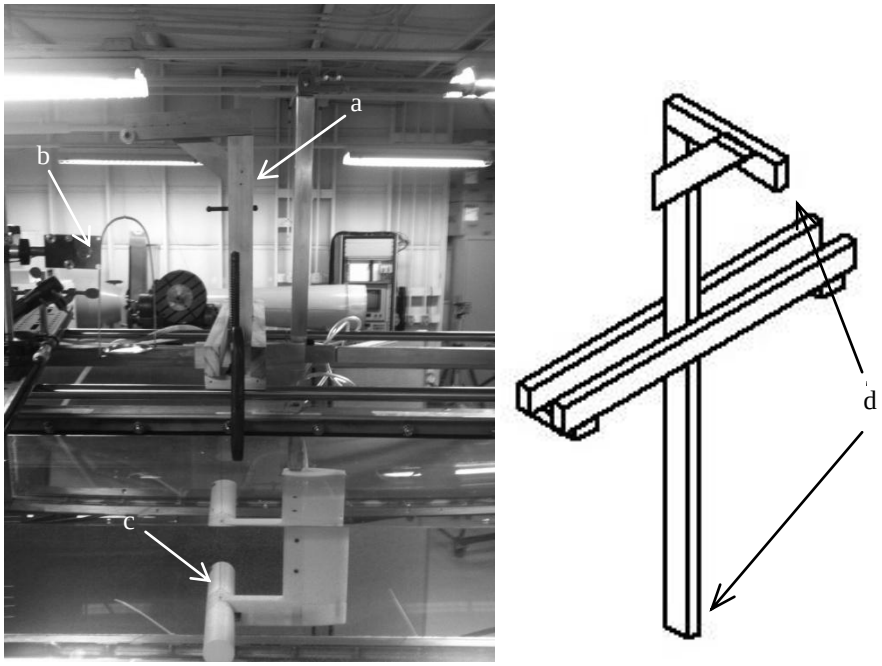

Figure 30. Force Balance Calibration Device Position 1. Shown in the figure are the following: a) force balance calibration device, b) weight basket, c) attachment point to models, and d) pulley locations.

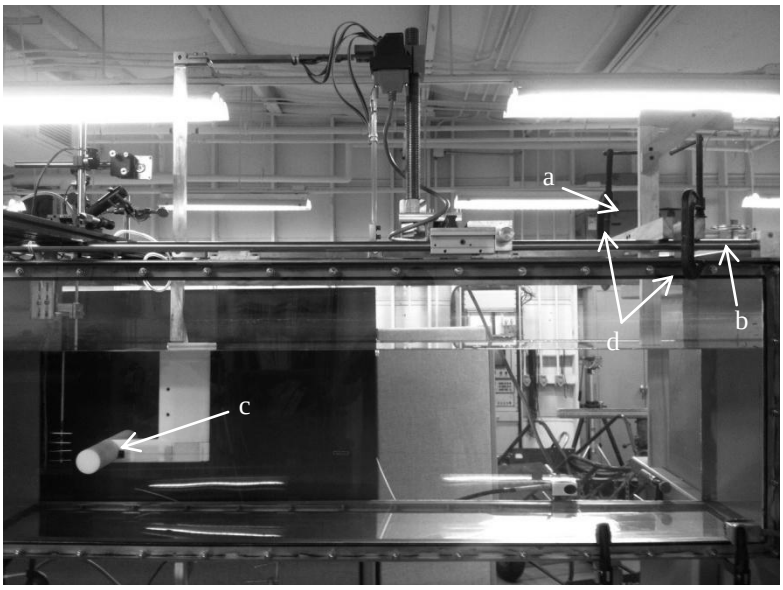

Figure 31. Force Balance Calibration Device Position 2. Shown in the figure are the following: a) force balance calibration device, b) weight basket, c) attachment point to models, and d) clamps attaching force calibration device.

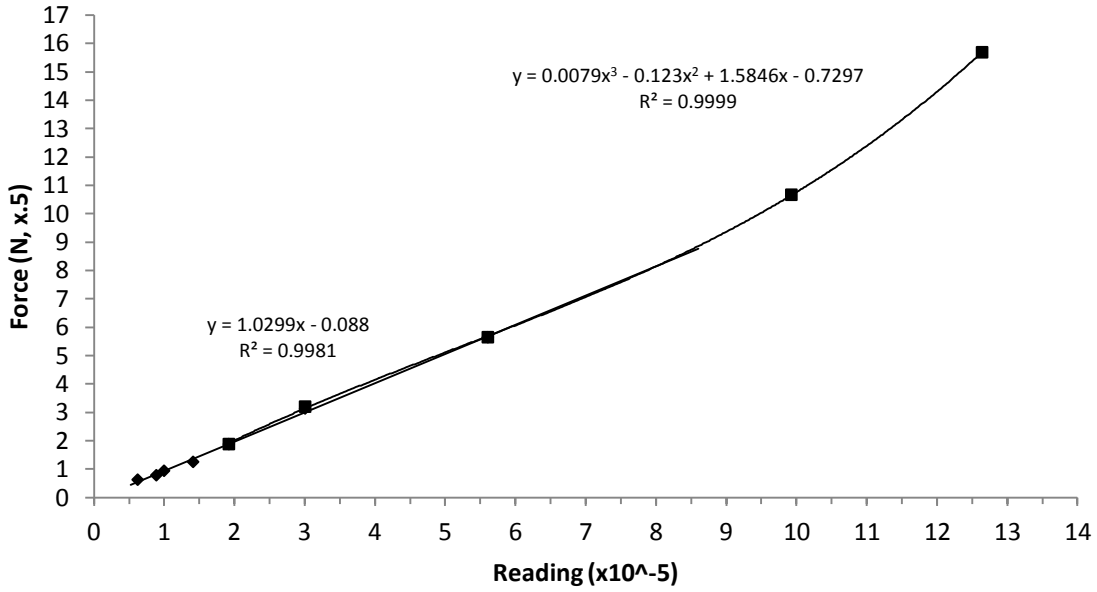

Figure 32. Horizontal Balance Bar Calibration. The majority of the calibration is linear with a nonlinearity at the upper end. The force for this bar directly corresponds to lift.

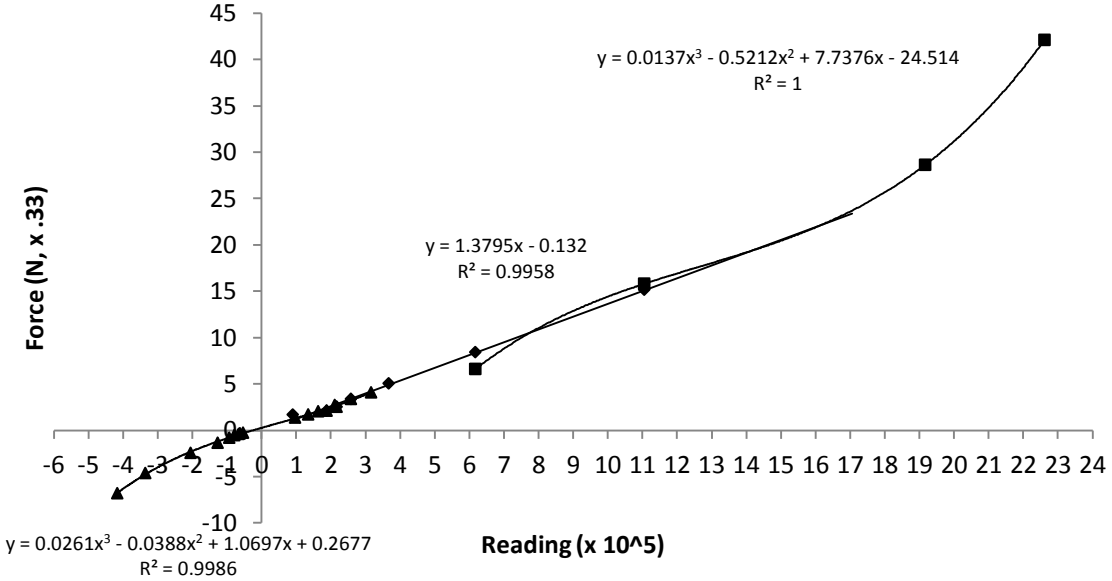

Figure 33. Vertical Balance Bar Calibration. The majority of the calibration is linear with nonlinearity at the upper and lower ends. The force for this bar corresponds to the force applied to the center of the C-flex connection at the bottom of the vertical bar.

Figure 34. Tunnel Motor Controller. Water tunnel flow speed was initiated and changed by manually adjusting the knob on the bottom left face of the controller.

In Equation 37, q represents a quantity, dependent upon $m, \ldots, n$, for which the uncertainty is sought. Applying Equation 37 to Equation 36, the uncertainty in flow speed was calculated as shown in Equation 38.

$$\delta v = \sqrt{\left(\frac{\partial v}{\partial s_1}\delta s_1\right)^2 + \left(\frac{\partial v}{\partial s_2}\delta s_2\right)^2 + \left(\frac{\partial v}{\partial t_1}\delta t_1\right)^2 + \left(\frac{\partial v}{\partial t_2}\delta t_2\right)^2} \tag{38}$$

The flow meter calibration curve is shown in Figure 35. Error in flow speed ranged from $\pm 0.6\%$ to $\pm 2.5\%$. Error increased with increasing speed due to the decreasing time involved in calibration at the higher speeds.

The models' rpm was recorded using a World-Beam® QS30 photoelectric sensor, shown in Figure 36, along with polarized retroreflective tape, shown in Figure 37, affixed to the models. The sensor emitted an electrical signal when it received a reflection of its output beam from the retroreflective tape. The data acquisition system counted the number of signals received over a given period of time. Data were collected over $10\ s$ increments yielding an uncertainty of $\pm 6\ rpm$. There was no uncertainty at $0\ rpm$, when the motor was not running. With the motor driving the cylindrical bodies, rpm uncertainty ranged from $\pm 5.6\%$ at the lowest rpm to $\pm 0.7\%$ at the highest rpm. Flow speed, v, and rpm were used in the calculation of α as shown in Equation 39.

$$\alpha = \frac{v_r}{v} = \frac{2\pi r_{avg} rpm}{60v} \tag{39}$$

Uncertainties in α were calculated by substituting Equation 39 into Equation 37. They are presented in Chapter 4. Balance reading, flow speed, and rpm data were collected for all flow conditions. Balance readings taken during a no-flow and no-rotation condition were used to find a zero lift and zero drag offset that was applied to the balance readings for all other flow conditions. Additional zeroing was necessary for the horizontal balance bar readings (lift bar) to remove no-rotation reading changes as flow speed was increased. A linear interaction between the lift bar and motor rpm, quantified using data from the no-

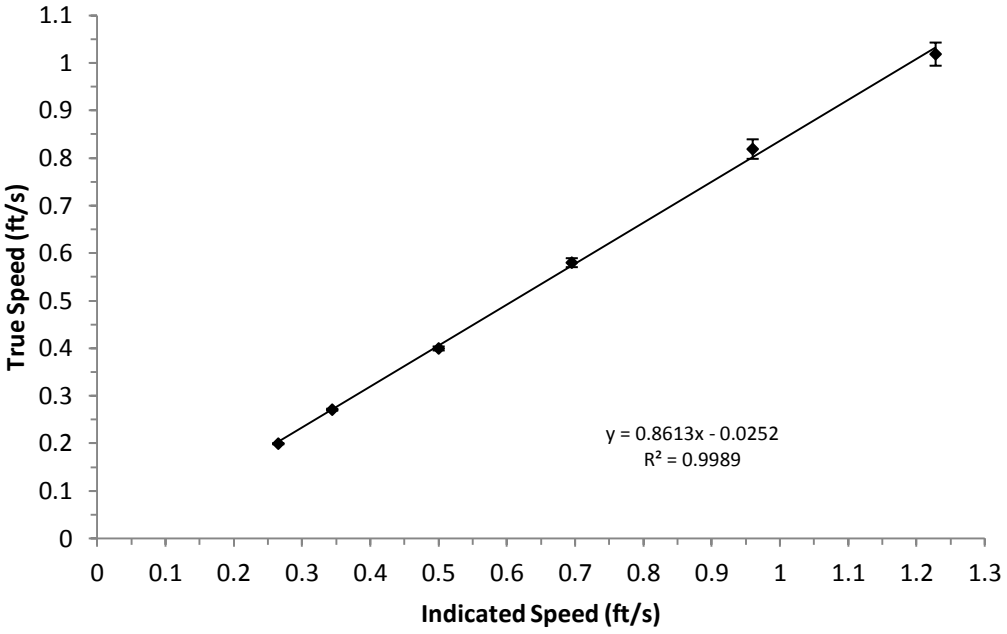

Figure 35. Flow Speed Calibration. Error bars indicate increasing error with increasing speed. The increased error is due to smaller time differences during calibration at higher speeds.

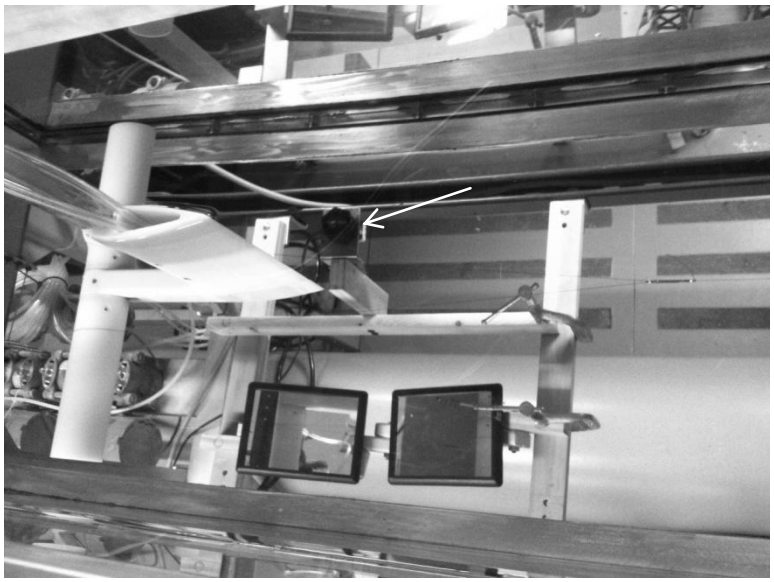

Figure 36. World-Beam® QS30 Photoelectric Sensor. The sensor, identified by the arrow, is mounted beneath the tunnel and is directed upwards through the bottom of the tunnel test section. The sensor is shown from a perspective above the tunnel.

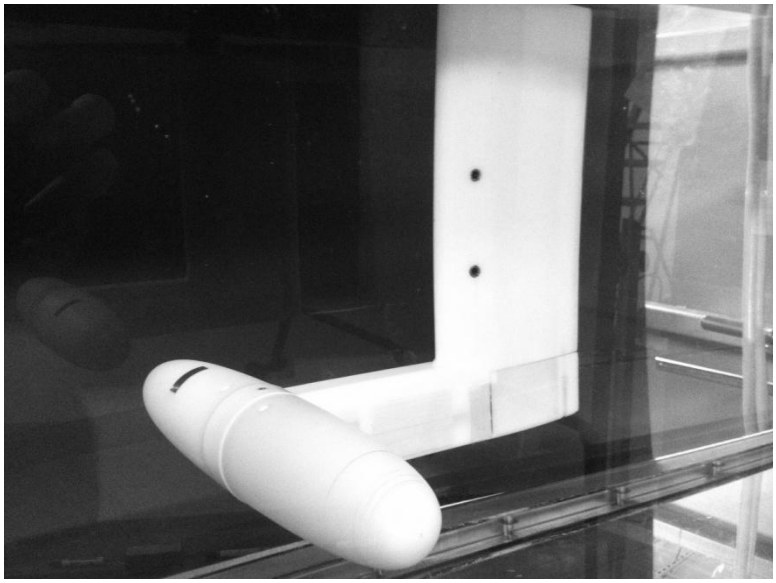

Figure 37. Retroreflective Tape. The BBOR models are installed with the retroreflective tape strip for rpm measurement.

flow, with-rotation condition, was removed for all conditions. The author suspects this downforce was due to induced downward flow over the rectangular portion of the CNF aft of the models. The fact that the downforce was greater for the BBOR than for the CDCC supports this, since induced flow speeds should be higher near the CNF where the BBOR radius is larger than that of the CDCC. The difference in induced flow at the CNF is visualized in the next chapter. Interaction between the drag bar and motor rpm was inconsistent and was not used to correct balance readings. The lack of a similar interaction for the drag bar could be due to the fact that induced flow in the drag direction flowed over the streamlined vertical portion of the model mount resulting in minimal forces. Balance readings were then converted to applied forces from which lift, drag, force coefficients, and force ratios were then calculated. Lift was calculated directly from the calibration equations presented in Figure 32. Drag was calculated first by finding the force applied to the drag bar, F, from the calibration equations in Figure 33 and then substituting that force, along with lift, into Equation 40, which provides drag based upon the balance geometry.

$$D = \frac{16.2063F + 4.686L}{28.9861} \tag{40}$$

The coefficients of lift and drag were calculated using Equations 41 and 42 respectively.

$$C_L = \frac{2L}{\rho v^2 S} \tag{41}$$

$$C_D = \frac{2D}{\rho v^2 S} \tag{42}$$

The planform area, S, of the models was calculated similarly to calculating the planform area of a fixed wing when it is connected to a fuselage. The rectangular area of the fuselage connecting the wing on one side to the wing on the other side is often included in the wing's planform area. The same method was used for the cylindrical models. The area of the CNF between the models was included in the planform area calculation. For the CDCC, this area was simply a rectangle with a chord equal to the diameter of the

CDCC and a span equal to the width of the model mount. For the BBOR, the span was identical, but the chord was equal to the maximum diameter, $2r_0$ where $r_0 = 2.63\ cm$. Since the models had equal average radii, $r_{avg} = 2.3\ cm$, the planform area of the BBOR was slightly larger than that of the CDCC. The increase in planform area was approximately 1%. The uncertainty for planform area was $\pm 0.06\%$. Uncertainty in C_L and C_D was calculated by substituting Equation 41 and Equation 42 into Equation 37. L/D was calculated directly by dividing lift by drag. Uncertainties in L/D was calculated by substitution into Equation 37. The uncertainties are presented in Chapter 4. The following plots presented in Chapter 4 were then created: $C_L\ vs\ \alpha$, $C_D\ vs\ \alpha$, and $L/D\ \ vs\ \alpha$. Identification of $C_{L_{max}}$ and $(L/D)_{max}$ was made for each model within specific ranges of α for each Re. Comparisons were made between the CDCC and the BBOR. Flow visualizations were captured by illuminating streams of flouriscene dye with a laser sheet spread along the longitudinal axis of the body at selected spanwise locations. The photographs were postprocessed to highlight the contrast between the dye and the water. The visualizations were used for qualitative analysis.

Chapter 4

Results and Discussion

Data were collected for force balance calibration and for each set of models over a three day period. Each model was tested at seven flow speeds from 0 to 0.46 m/s and a range of rotational speeds from 0 to 900 rpm. The combinations of flow speeds and rotational speeds resulted in Re ranging from 6×10^2 to 2.2×10^4 and α ranging from 0 to 180. The results of testing are presented and discussed in subsequent sections.

Results

Force coefficients. Coefficient of lift and coefficient of drag values were calculated by the process outlined in Chapter 3. Results have been presented by Re, beginning with data for the highest Re. Figure 38 presents the data for $Re = 2.2 \times 10^4$. Although the scale of the figure may not immediately seem appropriate, it was adjusted for comparison with the data for other values of Re. Figure 38 revealed that C_D for both models dropped as α was initially increased above 0. The minimum drag coefficient, $C_{D_{min}}$, observed for the CDCC was 0.8 and occurred at $\alpha = 1.2$. This was followed by a nearly linear increase in C_D as α approached 5. The slope of the $C_D vs. \alpha$ curve will henceforth be referred to as C_{D_α}. C_L for both models exhibited an approximately linear increase with α after which the slope of the data, C_{L_α}, began to decrease at $\alpha \sim 3$. Since C_{L_α} remained positive over the $0 \leq \alpha \leq 5$ range possible at this Re, the maximum C_L for the CDCC was approximately 4.1; however, $C_{L_{max}}$ was not apparent. The C_D and C_L curves for both the CDCC and BBOR were similar, although C_D at $\alpha = 0$ for the CDCC was 4% higher and C_{L_α} at $\alpha \sim 1.2$ for the CDCC was double that of the BBOR.

The next set of data corresponded to $Re = 1.4 \times 10^4$. As seen in Figure 39, the same trends for C_D and C_L were evident; however, the curves were extended to a maximum α of approximately 7.3 due to the reduced flow speed. The initial decrease to a minimum C_D witnessed at $Re = 2.2 \times 10^4$ was not observed due to the inability to achieve lower values of α at this and all lower values of Re. Minimum α was determined

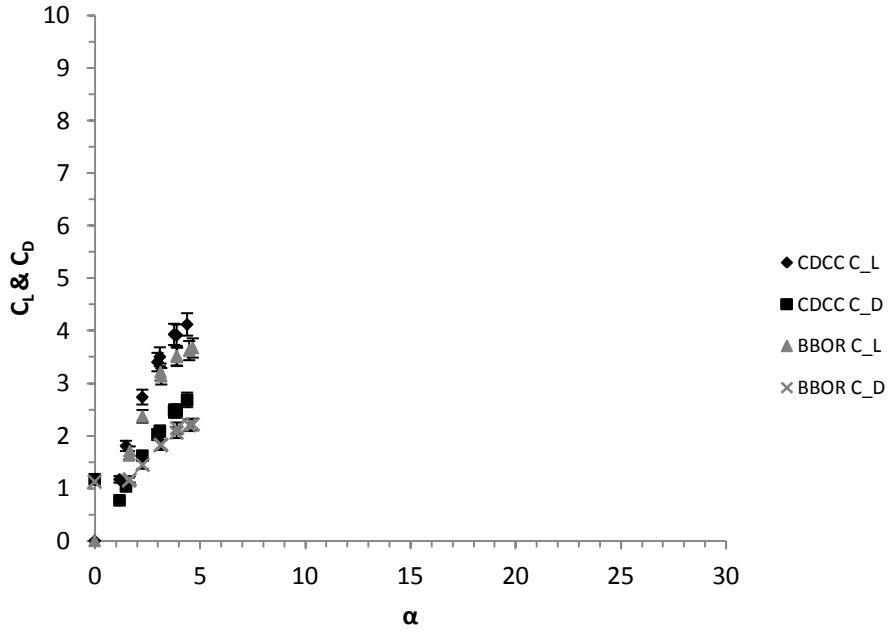

Figure 38. Force Coefficients at $Re = 2.2 \times 10^4$.

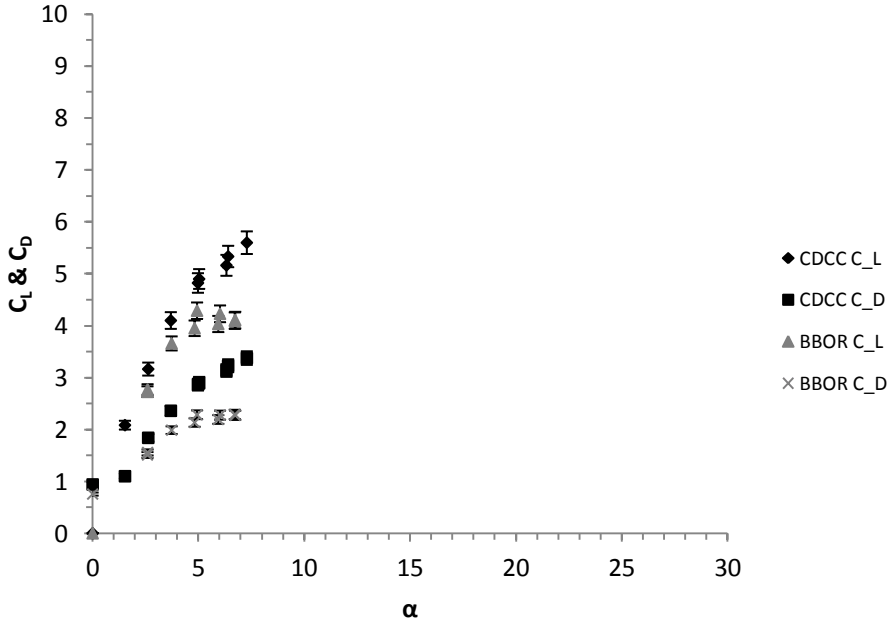

Figure 39. Force Coefficients at $Re = 1.4 \times 10^4$.

by the minimum sustainable rpm, approximately $100\ rpm$, of the motor. C_{D_α} and C_{L_α} appeared to remain positive for all four curves. The slopes continued to decrease for all curves with the BBOR curves decreasing more rapidly. The maximum C_L for the CDCC was increased to approximately 5.6. $C_{L_{max}}$ was still not apparent since C_{L_α} remained positive. For a constant value of α, C_L at $Re = 1.4 \times 10^4$ was higher than C_L at $Re = 2.2 \times 10^4$ by 7%. No significant differences were observed between C_D at fixed α for the two Re although the CDCC exhibited a 6% increase in drag for $\alpha = 2$.

The next Re tested was approximately 1.0×10^4. The trend established by the previous two values of Re was continued to a maximum α of 10.6 as shown in Figure 40. The linearity of the C_D and C_L curves with α seemed to have again been established albeit at lower values of C_{D_α} and C_{L_α}. The maximum C_L for the CDCC was increased to approximately 6.1 at $\alpha = 10.6$.

As Re was decreased to 4.0×10^3, C_{D_α} and C_{L_α} plateaued, became negative, then once again became positive for both models as presented in Figure 41. C_{D_α} exhibited similar behavior for both models. The maximum C_L for the CDCC was increased to approximately 7.7 at $\alpha = 23.4$.

Reduction of Re to approximately 2.4×10^3, as presented in Figure 42, continued the trends shown for the previous Re. The maximum C_L for the CDCC was increased to approximately 8.4 at $\alpha = 34.9$. A major difference observed at this Re was that the maximum C_L for the BBOR, although still less than that for the CDCC, became much closer to the maximum $C_L$for the CDCC.

The lowest and final Re tested was 6.0×10^2, approximately two orders of magnitude smaller than the highest Re. Figure 43 shows that data scatter and increased uncertainty at this low Re made trends more difficult to discern; however, positive C_{D_α} and C_{L_α} continue for both models. For the first time, the maximum C_L value for the BBOR was higher than that for the CDCC. Maximum C_L for the BBOR was 77 at $\alpha = 184$.

Lift to drag ratios. Lift to drag ratios were calculated and plotted for the range of α at each Re. Data for $Re = 2.2 \times 10^4$ are presented in Figure 44. The lift to drag ratios

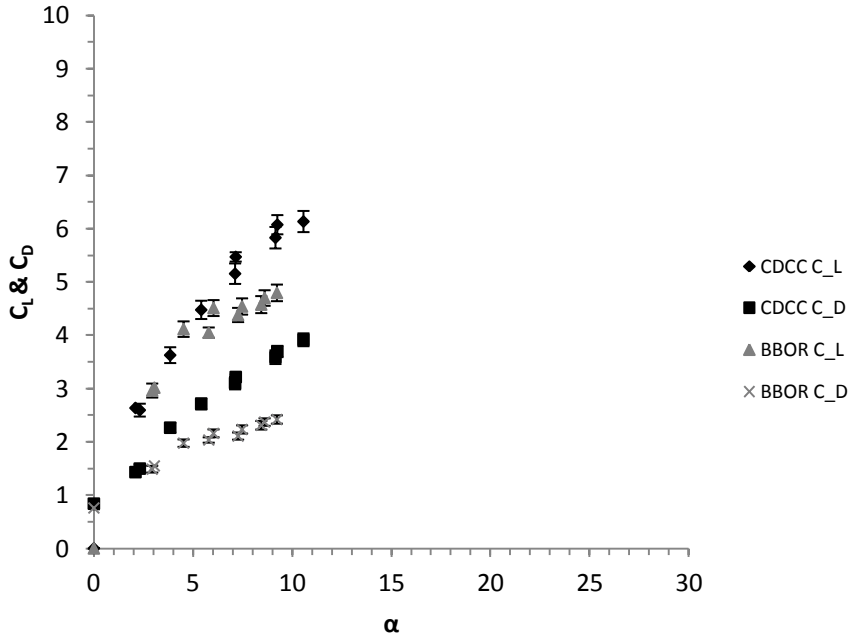

Figure 40. Force Coefficients at $Re = 1.0 \times 10^4$.

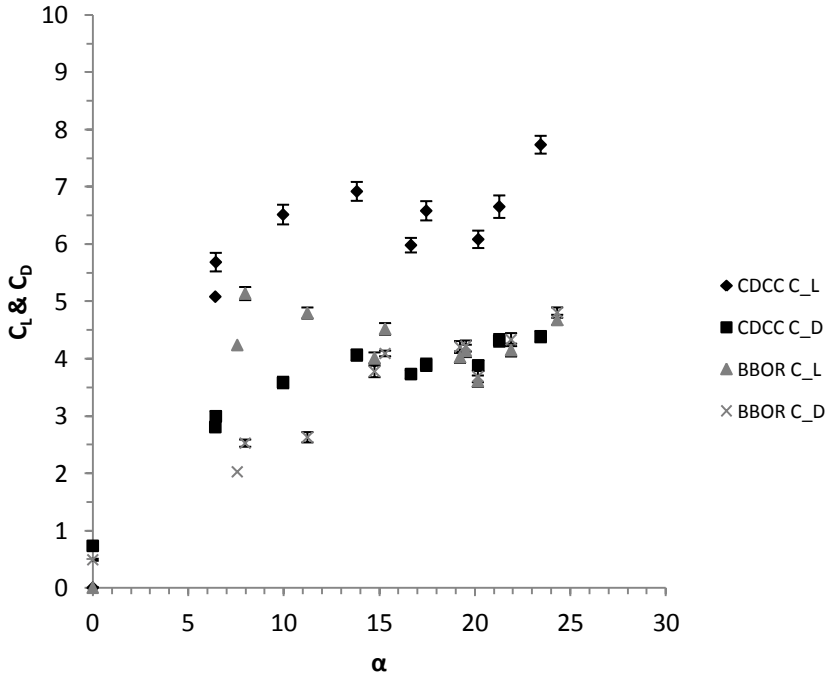

Figure 41. Force Coefficients at $Re = 4.0 \times 10^3$.

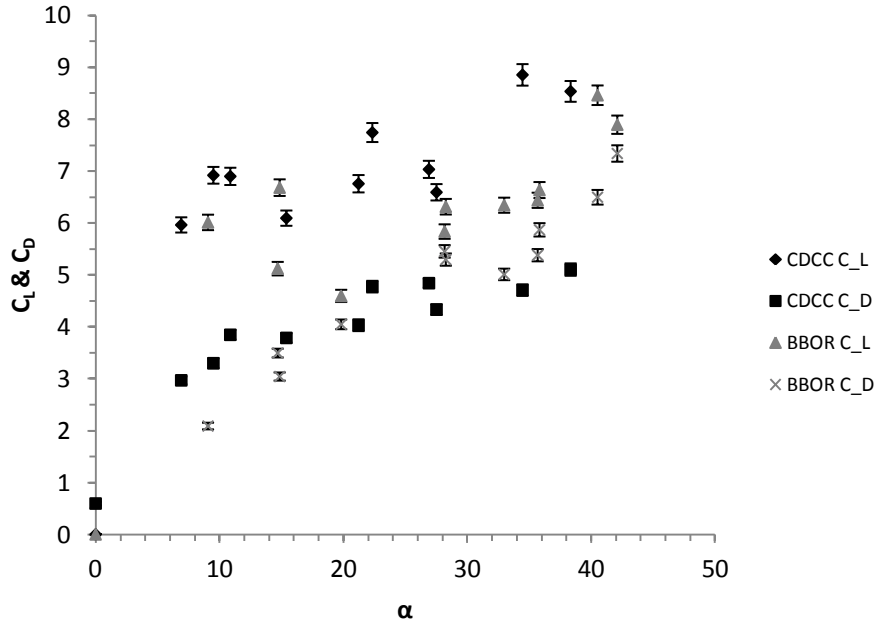

Figure 42. Force Coefficients at $Re = 2.4 \times 10^3$.

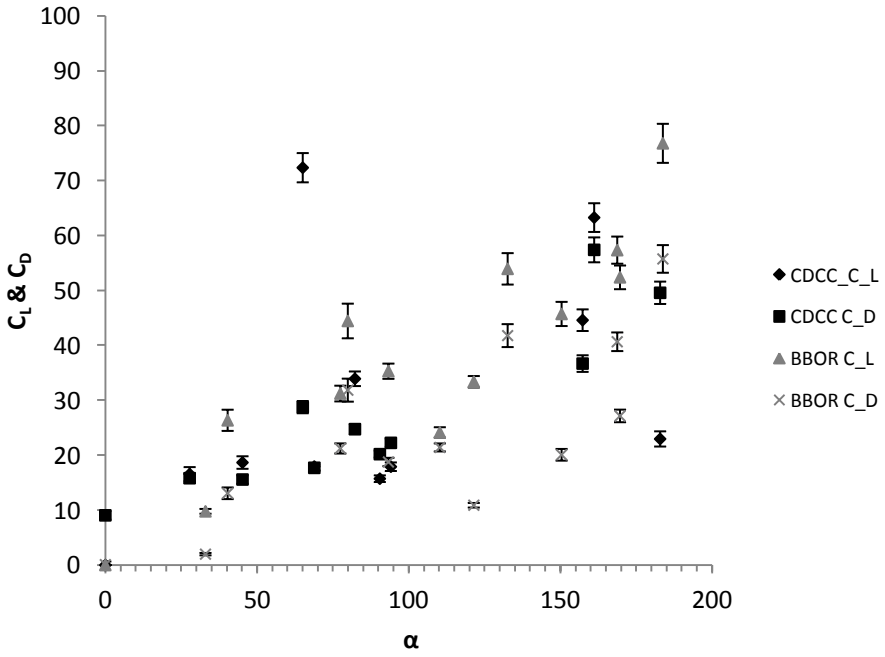

Figure 43. Force Coefficients at $Re = 6.0 \times 10^2$.

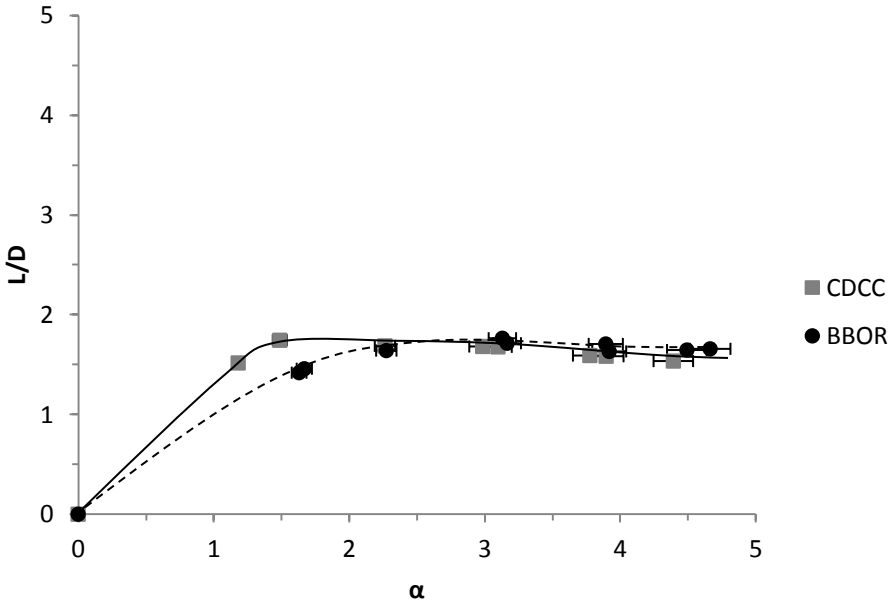

Figure 44. L/D at $\mathrm{Re} = 2.2 \times 10^4$.

for both the CDCC and the BBOR increased to a maximum of approximately 1.8 and plateaued at this value up to the maximum achievable α. The slope of the lift to drag curve of the CDCC was initially steeper than that of the BBOR; however, no apparent difference in $(L/D)_{max}$ was apparent.

The data for $Re = 1.4 \times 10^4$, shown in Figure 45, exhibited similar trends extended to higher α; although, $(L/D)_{max}$ increased to approximately 1.9. The slope of the lift to drag curve for the CDCC again was initially higher than that of the BBOR. The CDCC's L/D curve peaked at $\alpha = 2.6$, decreased, and leveled at $L/D = 1.7$. Another notable difference was at $\alpha = 3.2$ where the L/D for the BBOR exceeded that of the CDCC and continued to do so throughout the remainder of the α range.

This trend was confirmed at $Re = 1.0 \times 10^4$ as shown in Figure 46. L/D for the BBOR again rose above that of the CDCC from $\alpha = 2.2$ throughout the remainder of the α range tested. The margin by which the BBOR's L/D exceeded that of the CDCC's L/D increased within this range. The L/D for each model did exhibit a trend of converging toward a common value at higher α. The $(L/D)_{max}$ for the BBOR was approximately 2.1.

At $Re = 4.0 \times 10^3$ $(L/D)_{max}$ for the BBOR remained constant at 2.1 as can be seen in Figure 47. L/D for the BBOR continued to rise above that of the CDCC for a slightly different range, $4.1 \leq \alpha \leq 11.7$. Beyond this range of α, L/D for the BBOR rapidly decreased to approximately 1 while L/D for the CDCC decreased only slightly and exhibited an increase for $\alpha > 21$.

At $Re = 2.4 \times 10^3$ $(L/D)_{max}$ for the BBOR increased to 2.9 as can be seen in Figure 48. L/D for the BBOR rose above that of the CDCC for the range, $3.9 \leq \alpha \leq 15.8$. L/D for the BBOR and CDCC exhibited similar trends as with the higher Re yet again extended to higher α at the lower flow speed.

As with the data for force coefficients at $Re = 6.0 \times 10^2$, data scatter at this flow speed prevented clear curves from being created, as seen in Figure 49; however, the data indicated that L/D for the BBOR was above that of the CDCC throughout the majority of the large α range. $(L/D)_{max}$ for the BBOR was 4.9 ± 0.6 at $\alpha = 33$.

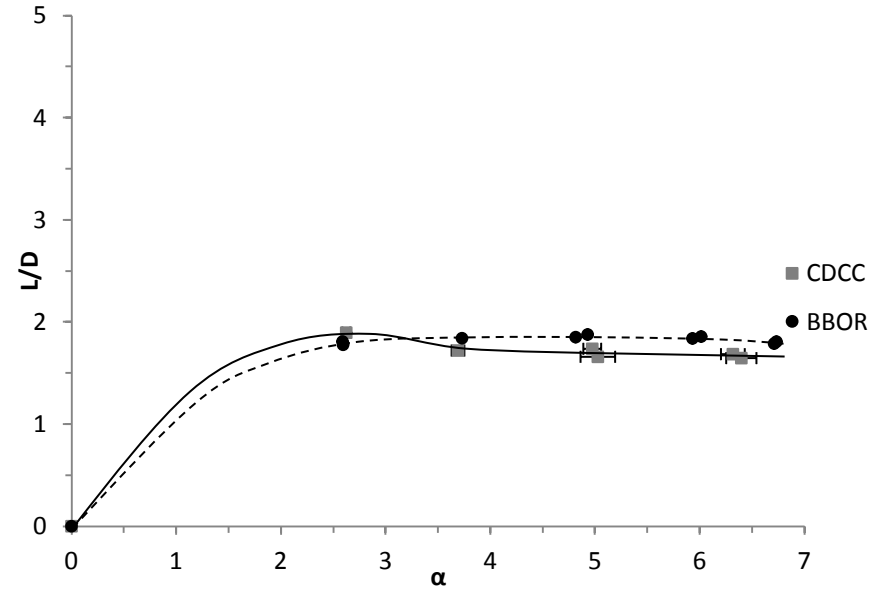

Figure 45. L/D at $\mathrm{Re} = 1.4 \times 10^4$.

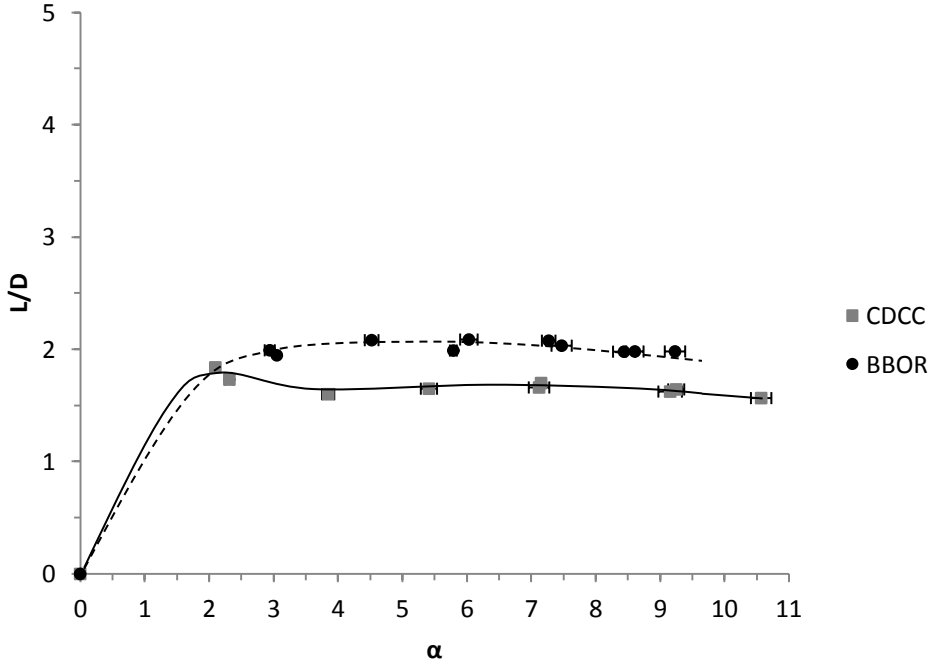

Figure 46. L/D at $\mathrm{Re} = 1.0 \times 10^4$.

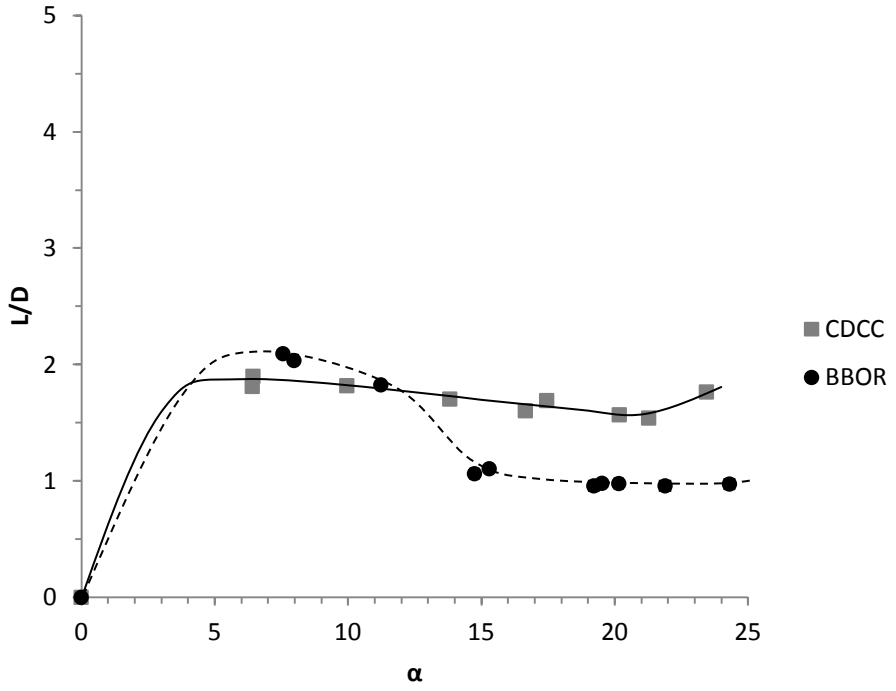

Figure 47. L/D at $\mathrm{Re} = 4.0 \times 10^3$.

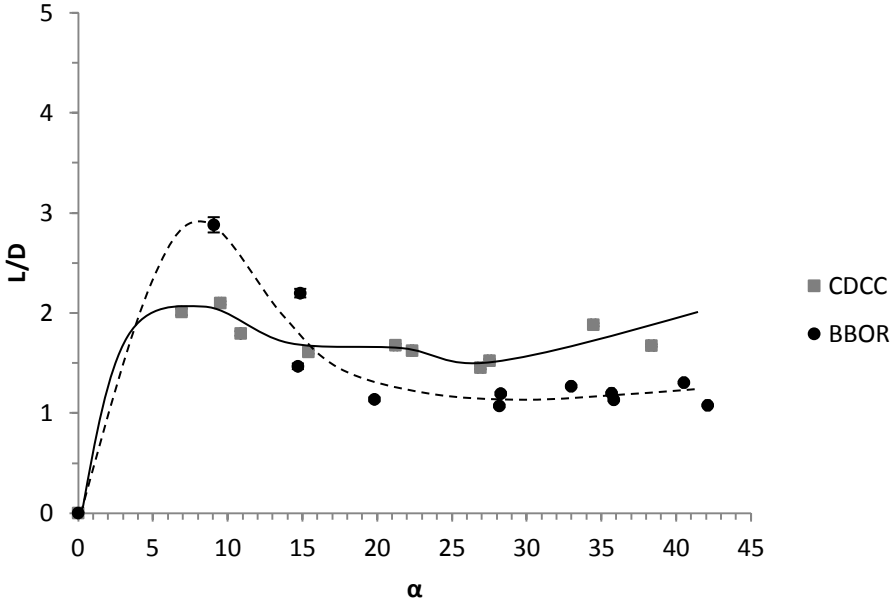

Figure 48. L/D at $\mathrm{Re} = 2.4 \times 10^3$.

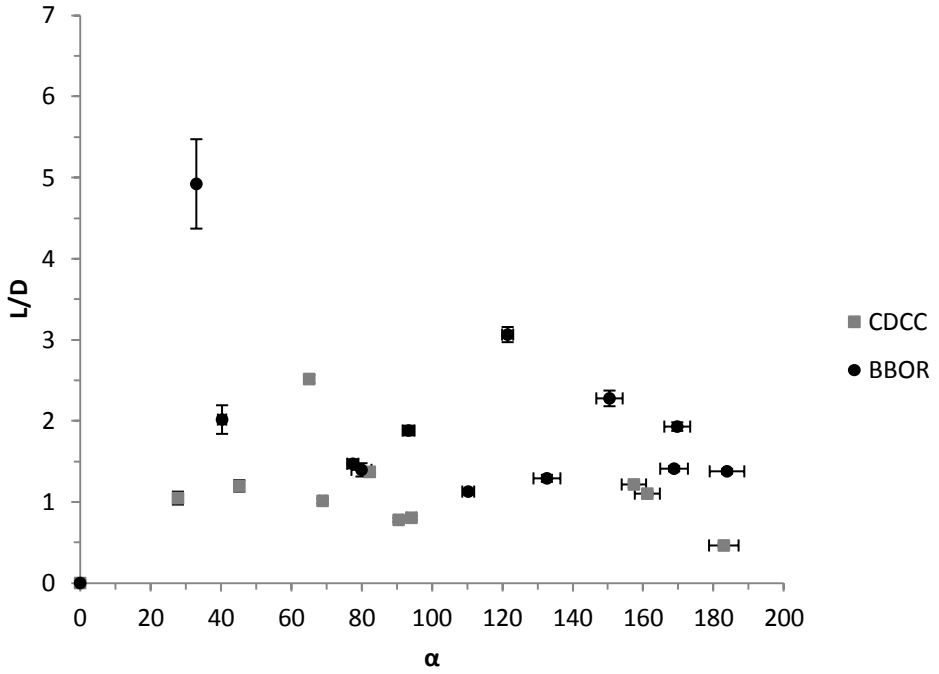

Figure 49. L/D at $\mathrm{Re} = 6.0 \times 10^2$.

Discussion

Force coefficients. As seen in Figures 40 through 44, zero rotation C_D for the BBOR was consistently lower than that for the CDCC. The C_D of each arrangement, at the highest Re tested, was seen to drop with the start of rotation followed by a continual increase as α increased. This decrease in drag is undoubtedly due to the decrease in pressure drag caused by flow separation over the blunt circular cross section of the cylinders. The energy added to the flow by the rotating bodies allowed the boundary layer to remain attached as seen in Figure 50. C_L also increased with α, although a plateau was discovered at $\alpha \sim 10$. C_L decreased until $\alpha \sim 15$ beyond which it increased for the tested values of Re. For fixed α, C_L for the models varied with Re as shown in Figure 51 and Figure 52. For the values of α evaluated, C_L for the BBOR increased with decreasing Re, with the exception of a decrease between $\mathrm{Re} = 1.4 \times 10^4$ and $\mathrm{Re} = 1.0 \times 10^4$ at $\alpha = 4$. C_D variation with Re, for fixed α, is shown in Figure 53 and Figure 54. For the values of α evaluated, C_D for the BBOR remained constant or decreased with decreasing Re, with the exception of an inecrease between $\mathrm{Re} = 1.0 \times 10^4$ and $\mathrm{Re} = 4.0 \times 10^3$ at $\alpha = 8$ and between $\mathrm{Re} = 4.0 \times 10^3$ and $\mathrm{Re} = 2.4 \times 10^3$ at $\alpha = 20$.

Lift to drag ratios. For the range of Re and α tested, the BBOR arrangement provided the local and global $(L/D)_{max}$. These values increased with decreasing Re as stated in the previous subsection. Within a noticeable range of α, for each Re, the BBOR arrangement was hydrodynamically more efficient than the CDCC arrangement, see Table 2. This was expected; however, for α outside of this range the CDCC was more efficient. According to Prandtl's lifting line theory, this should not be so. It is important to remember that Prandtl's analysis, which led to the optimal distribution of circulation, was not only inviscid but in essence 2-D. The lifting line, or superposition of vortex filaments, was infinitely thin thereby resulting in an infinite aspect ratio (AR). Given the 2-D nature of the theory, the analysis made no room for flow along the span of the lifting line. In reality the velocity and pressure patterns surrounding a 3-D lifting surface will

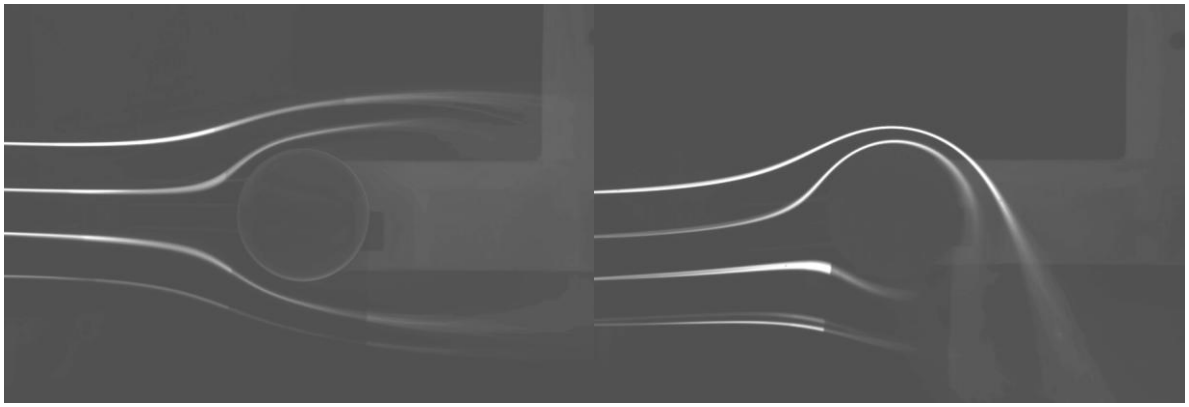

Figure 50. $Re = 4.0 \times 10^3$Streamlines about a Cylindrical body. The photo on the left is with $\alpha = 0$. The photo on the right is with $\alpha = 4.5$. Note the absence of flow separation about the rotating cylinder.

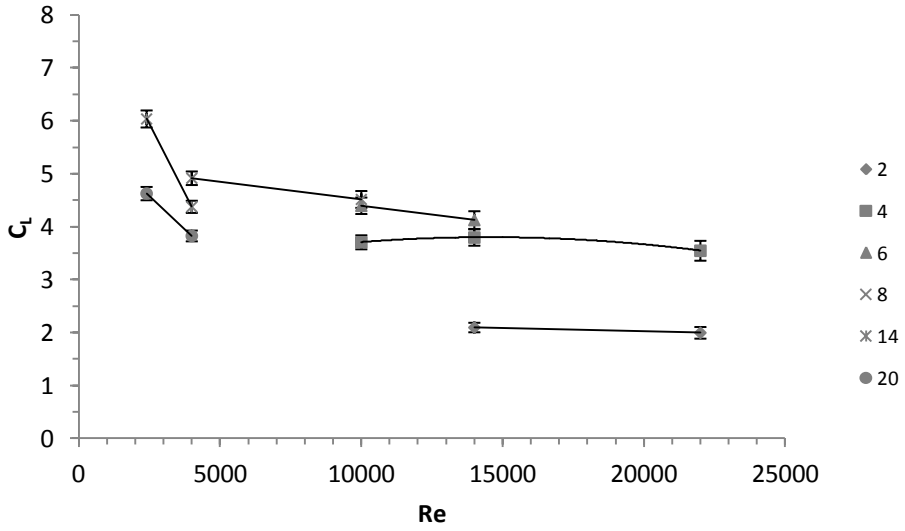

Figure 51. BBOR C_L $vs. Re$ for fixed α.

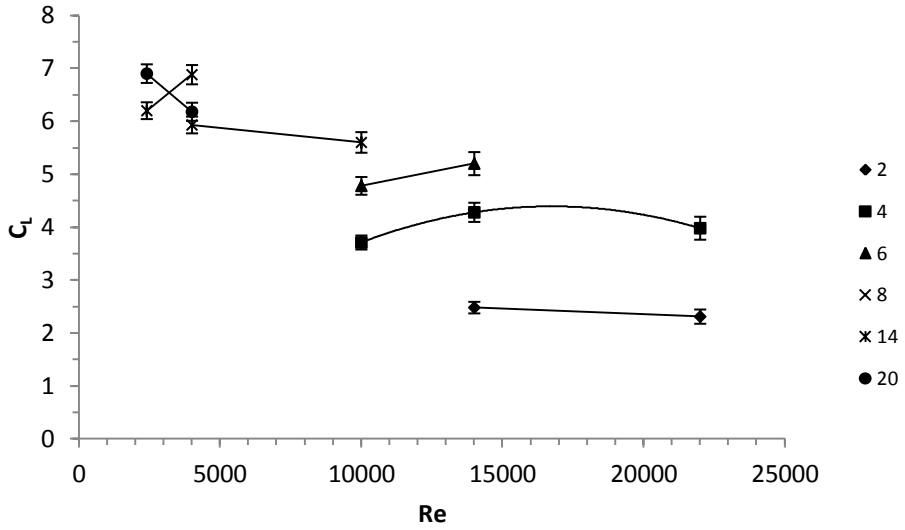

Figure 52. CDCC $C_L \; vs. Re$ for fixed α.

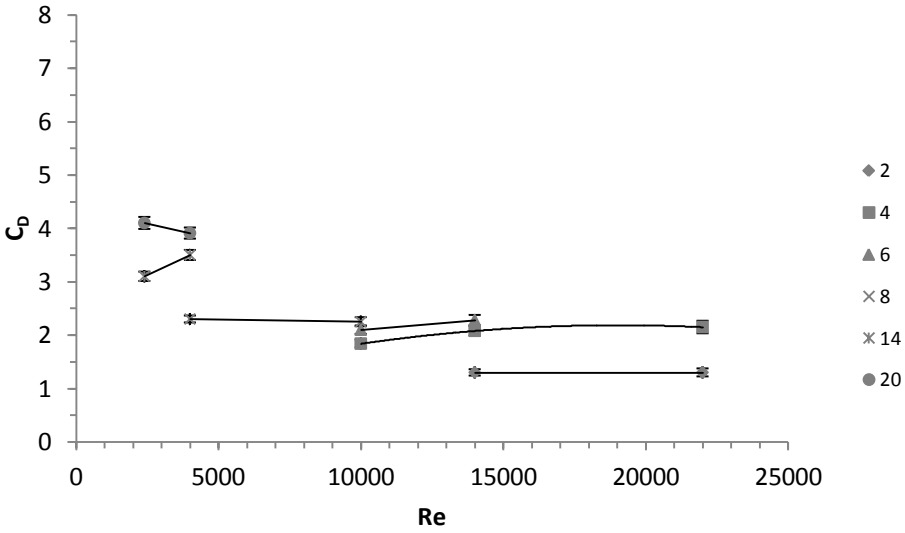

Figure 53. BBOR $C_D \; vs. Re$ for fixed α.

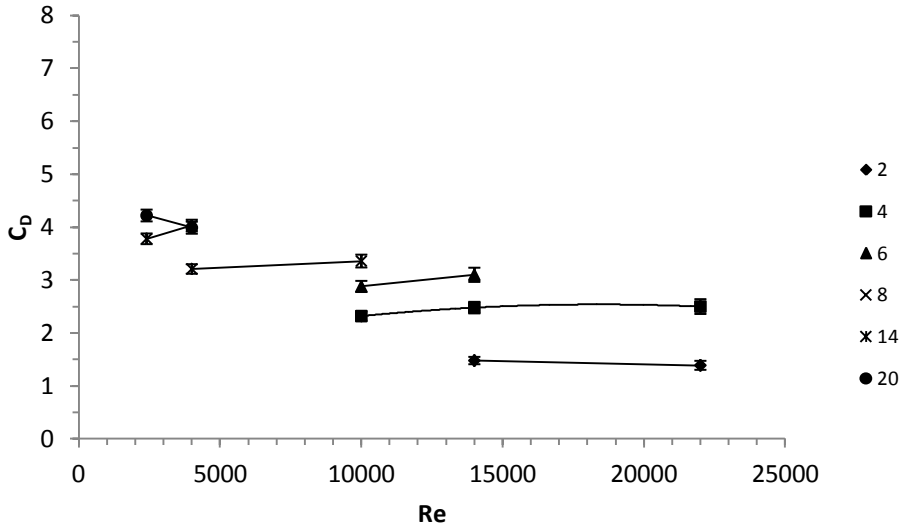

Figure 54. CDCC $C_D \; vs. Re$ for fixed α.

Table 2.

BBOR Optimum Conditions

Re	BBOR optimum α range	Local $(L/D)max$
2.2×10^4	$2.5 -$*	1.8
1.4×10^4	$3.2 -$*	1.9
1.0×10^4	$2.2 -$*	2.1
4.0×10^3	$4.1 - 11.6$	2.1
2.4×10^3	$4.0 - 15.5$	2.9
6.0×10^2	$< 50, 80 -$*	4.9

*BBOR L/D was higher at the maximum α for this Re.

distort the pattern predicted for a finite continuum of 2-D cross-sections. Higher pressures are allowed to equalize at the finite tips of the lifting surface causing a component of the flow to be along the span. For example if the CDCC were treated as a collection of 2-D sections, each section would impart the same circulation to the surrounding flow since each section had the same radius. Flow visualizations of the CDCC arrangement showed otherwise. Photographs were taken at $Re = 4.0 \times 10^3$ and $\alpha = 10$ for seven locations along the halfspan of the CDCC and the BBOR arrangements measured from the root of the models. The seven locations were $-0.125\ in$, $0.125\ in$, $0.5\ in$, $1.625\ in$, $2.75\ in$, $3.875\ in$, and $5\ in$. The photographs along with photograph positions are presented in Figure 55. The column on the left presents photographs of the CDCC. The column on the right presents photographs of the BBOR. The first photographs' locations, shown in the first row of Figure 55, were slightly inboard of the rotating model placing them $0.125\ in$ inboard of the outer edge of the CNF. The second photographs, the second row, were taken $0.125\ in$ from the root of the rotating models. The remaining five rows of photographs in Figure 55 present images at increasing spanwise locations moving toward the models' tips. Photograph location is indicated above and to the left of each photograph. Long exposure times were necessary in order to capture the necessary light in the darkened test location. The photographs were therefore time averages over $20\ s$ periods at each spanwise location. Turbulence diffused the dye streams on the backside of the bodies, but streamlines leading to the bodies were relatively well formed. Returning to the 2-D hypothetical example for the CDCC, comparison of the 2-D analytical result could now be made to with reality. The left column of Figure 55 could be viewed from top to bottom. Changes in the streamlines from one row to the next were instructive since they collectively provide a spanwise view of the models effect on the flow. Specifically the third and fourth streamlines, numbered from top to bottom, provided visible indications of the flow patterns about the bodies at each location due to their proximity to stagnation streamlines. The third streamline in the first row of the CDCC's images was close to a stagnation point, as seen by the spreading of the streamline about the surface. The next image, taken slightly outboard of the first, showed that the third streamline had moved above a stagnation point. The continued

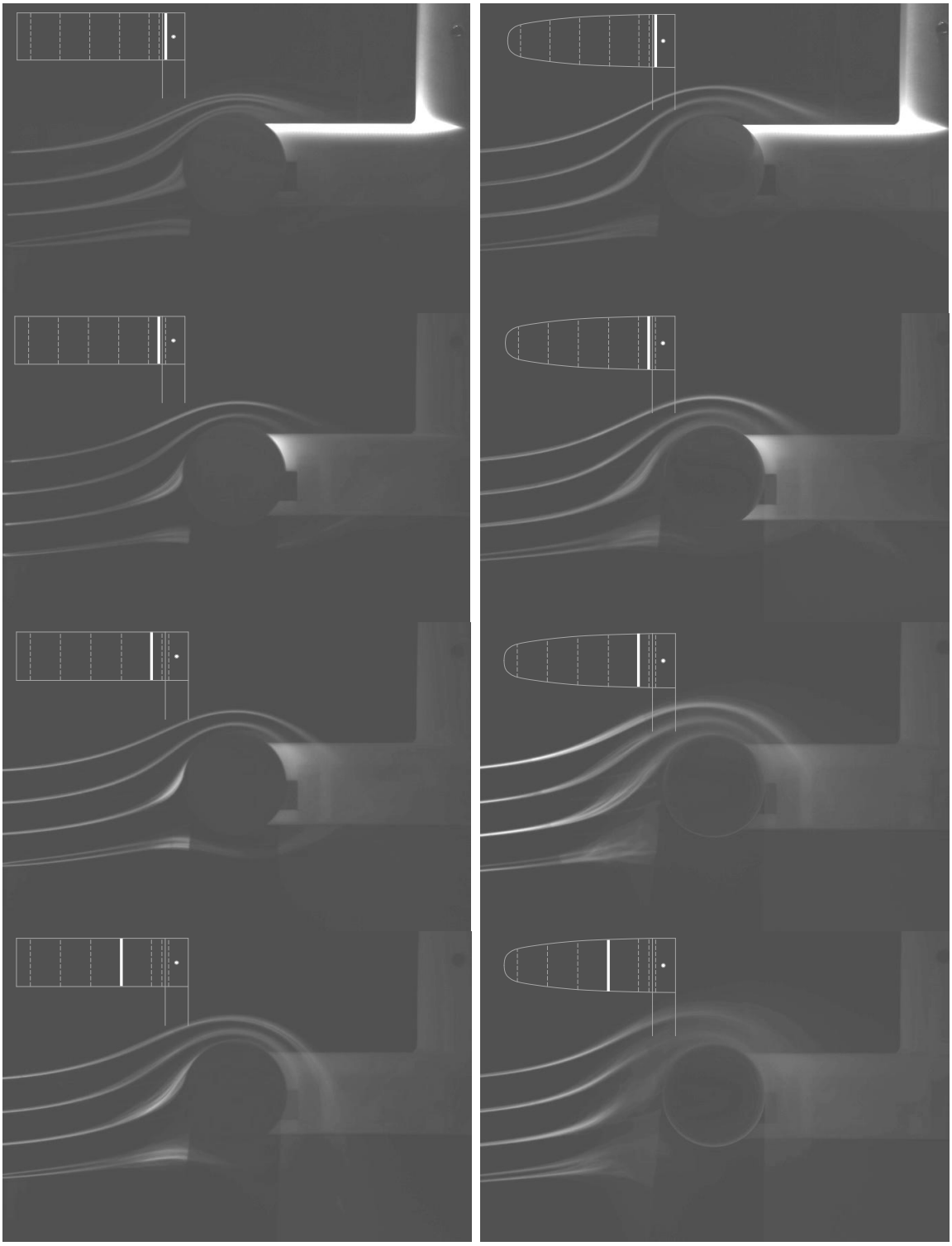

Figure 55. CDCC and BBOR Flow Visualizations. CDCC (left) and BBOR (right) positions are indicated by the solid lines on the diagram above and to the left of each photograph.

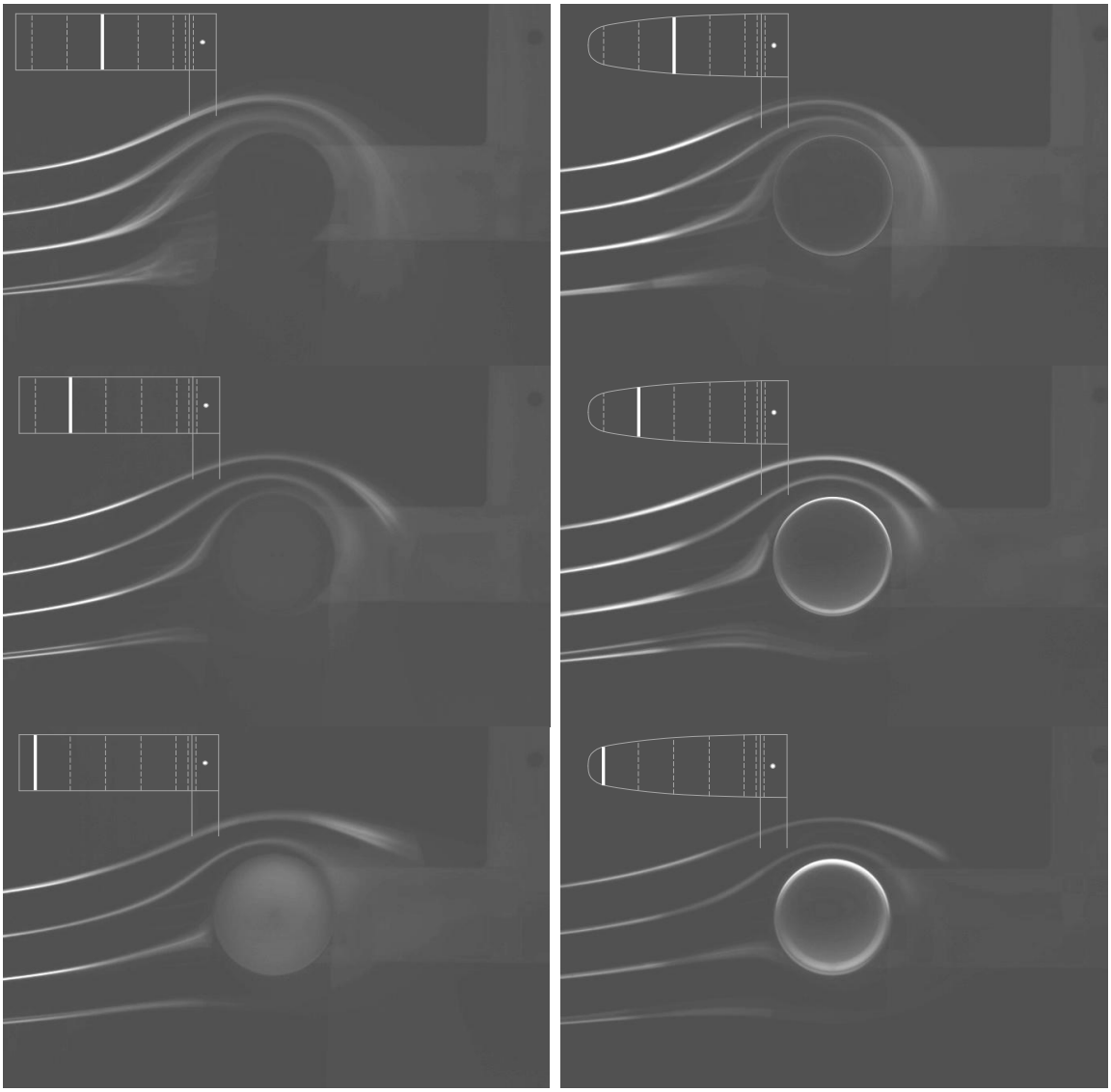

Figure 55 continued. CDCC and BBOR Flow Visualizations. CDCC (left) BBOR (right)

reduction in curvature of the third streamline over the next three images indicated increased circulation in the flow. The last two images showed a decrease in circulation about the CDCC with the last image showing the third streamline near to if not on a stagnation streamline. Although the CDCC's geometry was uniform in cross-section, the circulation distribution was not uniform. The nonuniformity near the CNF is understandable since this part of the body is not rotating. Circulatory flow is still imparted over this nonrotating section due to viscous interactions. The uniformity in flow towards the tips is lost due to spanwise flow allowed by the finite tips. Although not captured in a photograph, due to turbulent diffusion, the tip vortices could be seen rolling up behind the model tip. The photographs of the BBOR were similar to those of the CDCC; however, the circulation imparted to the flow near the CNF was greater owing to the large radius near the CNF. Likewise the circulation imparted to the flow near the tip was less due to the smaller radius.

BBOR circulation distribution. One of the central premises that guided this research was that the BBOR should produce an elliptical circulation distribution as described by Equation 19 and shown in Figure 17. Figure 55 provided qualitative data for visualizing the circulation distribution; however, a quantitative approach was developed by which the circulation distribution developed by the BBOR could be evaluated. Lifting line theory is based upon the integration of Kutta-Joukowski's theorem, stated by Equation 2. Integration of Equation 2 over a finite span with a known circulation distribution is presented in Equation 43.

$$L = \rho v \int_{-\frac{b}{2}}^{\frac{b}{2}} \Gamma(y) dy \tag{43}$$

Lift provided by the elliptical circulation distribution is calculated by substituting the elliptical distribution of circulation from Equation 19 into Equation 43 and integrating. This yields an equation for lift as shown in Equation 44.

$$L = \frac{\pi}{4} \rho v b \Gamma_0 \tag{44}$$

Substitution of Equation 44 and Equation 39, for α, into Equation 41 results in Equation 45 for calculating C_L as a function of α.

$$C_L = \frac{\pi}{4}\left(\frac{r_0}{r_{avg}}\right)^2 \alpha \tag{45}$$

The slope of $C_L\ vs.\ \alpha$ curves, C_{L_α}, is presented in Equation 46.

$$C_{L_\alpha} = \frac{\pi}{4}\left(\frac{r_0}{r_{avg}}\right)^2 \tag{46}$$

The BBOR models had $r_0 = 1.035\ in$ and $r_{avg} = 0.906\ in$ which yielded $C_{L_\alpha} = 1.025$. A line with this slope was placed on plots of the $C_L\ vs.\ \alpha$ data for the BBOR at $Re = 2.2 \times 10^4$ and $Re = 1.4 \times 10^4$ as shown in Figure 56 and Figure 57 respectively. The C_{L_α} of the data match that of the prediction, within the level of uncertainty, up to $\alpha \sim 3$, beyond which C_{L_α} began to decrease. This indicates for, $0 \leq \alpha \leq 3$, the BBOR does provide an elliptical distribution of circulation.

Karman vortex street. Although not photographically captured due to turbulent dissipation of the dye streams, a distinct von Karman vortex street was witnessed behind the models with $\alpha = 0$. At the higher Re tested, noticeable longitudinal oscillations were observed. Immediately upon initiating model rotation, the oscillations ceased. As was shown in Figure 50, the alleviation of flow separation with rotation led to the initial reduction in C_D as well as abating adverse longitudinal oscillations. Video evidence of this phenomenon was collected.

Model vibration. Rotating models supported at one end were susceptible to mass and mounting imbalance. These issues combined with short mounting shafts from the gearbox led to vibration when rotating the models. The aluminum models (both CDCC and BBOR) experienced vibration. The vibration was initially minimized by the

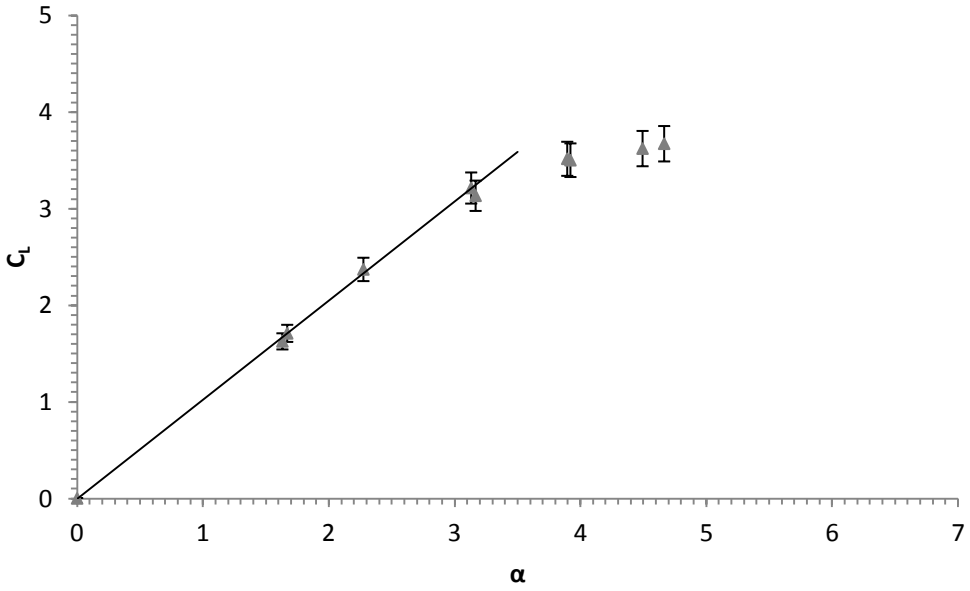

Figure 56. BBOR C_{L_α} at $Re = 2.2 \times 10^4$. C_L data for the BBOR on a line representing the theoretically predicted elliptical $C_L\ vs.\ \alpha$ curve of $C_{L_\alpha} = 1.025$.

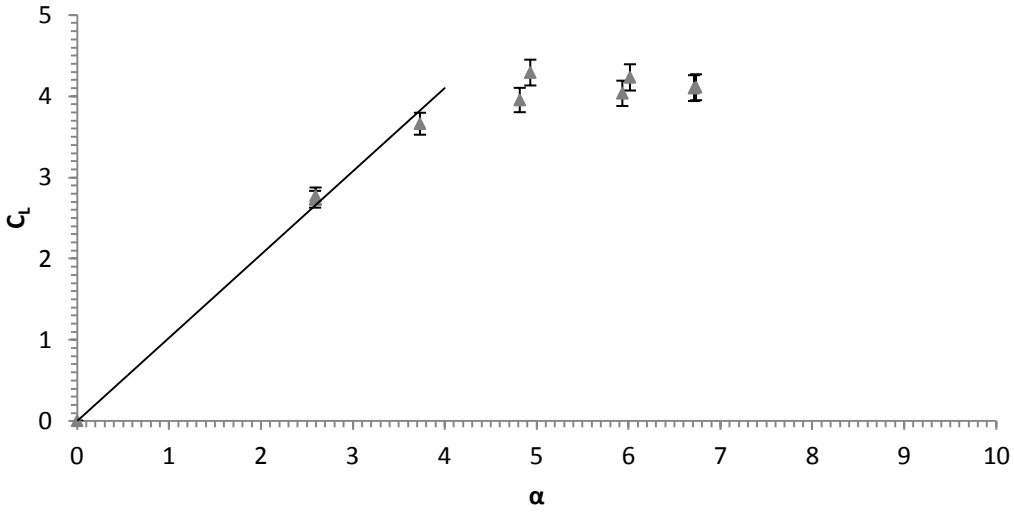

Figure 57. BBOR C_{L_α} at $Re = 1.4 \times 10^4$. C_L data for the BBOR on a line representing the theoretically predicted elliptical $C_L\ vs.\ \alpha$ curve of $C_{L_\alpha} = 1.025$.

following process. With the models spinning, a marker was brought close to the free end of one side until contact was made with the model leaving a mark. The process was repeated on the free end of the model on the other side. The models were then stopped, and the marks were aligned. This process was repeated with marks at spanwise locations further inboard. The result of this process was visually decreased yet still visible vibration. The next step was to reduce the mass of the models by constructing them out of Delrin® acetal resin. A minor difference between the aluminum and Delrin® models was that the bored holes were designed to be press fit onto the gearbox shafts albeit the set screw was still used. The Delrin® models exhibited similar vibration. Balancing, as was done with the aluminum models, only slightly alleviated vibration of the Delrin® models. One Delrin® model was overbored and fit loosely on the gearbox shaft. Upon tightening the set screw, the model was forced off center causing a vibration that could not be corrected by the first balancing technique. The next method to alleviate model vibration was to place two additional set screws at 120° in either direction from the original set screw. When care was taken while mounting the models and adjusting the set screws, the majority of perceptible vibration was removed.

Chapter 5

Conclusions and Recommendations

Conclusions

In conclusion rotating cylindrical bodies have been shown to produce force coefficients up to an order of magnitude larger than fixed wings at low Re. Lissaman (1983) showed $C_{L_{max}}$~1 for 2-D airfoils at low Re. Both cylindrical arrangements proved capable of significant increases above this value throughout the Re range tested. The BBOR arrangement exhibited hydrodynamic advantage, highest $(L/D)_{max}$, over the CDCC arrangement throughout the range of Re tested and within specific bands of α. 3-D end effects due to finite AR contribute to the difference between the 2-D analysis and the actual results.

The state of the art has been expanded by this work as follows: 1) a theoretical optimization of the cylindrical geometry used for lift production via the Robins-Magnus Effect was presented resulting in the biquadratic body of revolution (BBOR), 2) an experimental system to include a force balance and a mechanism for driving rotating cylinders in a water tunnel at low Re was presented, 3) the C_L, C_D, and L/D results from the comparison of CDCC and BBOR arrangements were presented in which the hydrodynamic advantage of the BBOR over the CDCC was demonstrated, 4) the increased effectiveness of the Robins-Magnus Effect at low Re was demonstrated by the increasing L/D values with decreasing Re, and 5) evidence that the BBOR created an elliptical circulation distribution was demonstrated by the BBOR's C_{L_α} matching that of the theoretical prediction. The latter three are significant to micro air vehicles (MAV), since MAVs operate at very low Re and could benefit from the increased efficiency of the BBOR.

Recommendations

The author's recommendations and plans for future research in this area are as follows. Surface roughness could be varied to highlight the viscous effects for rotating cylinders. The BBOR and other cylindrical bodies could incorporate fences at spanwise locations, including the tips, in an effort to minimize the 3-D effects along the span. Cylinders with linearly tapered distribution of radii could be evaluated as a compromise between the easily manufactured CDCC and hydrodynamically optimized BBOR. Numerical analysis could be performed on BBORs of various aspect ratios at low Re. Based upon flow visualizations presented in this document and those witnessed by the author while conducting research on this project, the turbulent nature of the flow aft of the models is a primary consideration. Appropriate turbulence models and grid regions need to be identified. Rotating cylindrical bodies could be incorporated in the trailing edges of control and lifting surfaces to provide flutter abatement at high speeds based upon the ability of rotating cylinders to minimize separation induced oscillations as witnessed during this project. Flow control could be investigated on fixed wings with integral rotating cylinders at the following locations: at the point of separation near the leading edge, at the maximum thickness location, at the flap hinge (to promote the Coanda effect).

The author has conducted preliminary research with a rotating cylinder embedded at the point of maximum thickness in a fixed wing. Initial wind tunnel data showed that the zero-α C_L was increased by 0.4. The entire lift curve was also increased by the same amount. This was a significant increase in C_L given that $C_{L_{max}} \sim 1$ was observed for the wing without rotation.

Another area of future research, which was one of the main applications inspiring the current research, was lift production for MAVs. The author has identified three areas upon which research could focus: 1) a fixed rotating cylinder providing lift with traditional fixed stabilizing and control surfaces; 2) multiple fixed rotating cylinders providing lift, stability, and control; and 3) rotating cylindrical lifting rotors. The author plans to begin with the former, a MAV with traditional fixed stabilizing and control

surfaces with lift supplied by fixed rotating cylinders. A final recommendation is to perform a detailed characterization of the UTSI force balance with the goal of developing an automated data acquisition system.

References

(2013). Retrieved June 29, 2013, from All Air Inc.: http://www.allair.com/micromotors.htm

Abbott, I. H., & von Doenhoff, A. E. (1959). *Theory of Wing Sections.* Mineola, NY: Dover.

Anderson, J. D. (2007). *Fundamentals of Aerodynamics* (5th Edition ed.). New York, NY: McGraw-Hill.

Aoi, T. (1955, February). The Steady Flow of Viscous Fluid Past a Fixed Spheroidal Obstacle at Small Reynolds Numbers. *Journal of the Physical Society of Japan, 10*(2), 119-129.

Badr, H. M., Coutanceau, M., & Dennis, S. C. (1990). Unsteady Flow Past a Rotating Circular Cylinder at Reynolds Numbers 10^3 and 10^4. *Journal of Fluid Mechanics, 220*, 459-484.

Bairstow, L., Cave, B. M., & Lang, E. D. (1923, July 20). The Resistance of a Cylinder Moving in a Viscous Fluid. *Philosophical Transactions of the Royal Society of London. Series A, Containing Papers of a Mathematical or Physical Character, 223*, 383-432. Retrieved March 28, 2012, from http://www.jstor.org/stable/91150

Breach, D. R. (1961). Slow Flow Past Ellipsoids of Revolution. *Journal of Fluid Mechanics, 10*, 306-314.

Burns, J. A., & Ou, Y.-R. (1993). *Effect of Rotation Rate on the Forces of a Rotating Cylinder: Simulation and Control.* NASA Langley Research Center, Institute for Computer Applications in Science and Engineering. Hampton, VA: National Aeronautics and Space Administration.

Carmichael, B. H. (1981). *Low Reynolds Number Airfoil Survey Volume I.* NASA-CR-165803, National Aeronautics and Space Administration, Langley, VA.

C-Flex Bearings Double End Bearing. (2010). Retrieved January 9, 2013, from C-Flex Bearings Co., Inc.: http://www.c-flex.com/dtable.html

Chen, Y.-M., Ou, Y.-R., & Pearlstein, A. J. (1993). Development of the Wake Behind a Circular Cylinder Impulsively Started into Rotary and Rectilinear Motion. *Journal of Fluid Mechanics, 253*, 449-484.

Chew, Y. T., Cheng, M., & Luo, S. C. (1995). A Numerical Study of Flow Past a Rotating Circular Cylinder Using a Hybrid Vortex Scheme. *Journal of Fluid Mechanics, 299*, 35-71.

Chou, M.-H. (2000). Numerical Study of Vortex Shedding From a Rotating Cylinder Immersed in a Uniform Flow Field. *International Journal for Numerical Methods in Fluids, 32*, 545-567.

Clift, R., Grace, J. R., & Weber, M. E. (1978). *Bubbles, Drops, and Particles.* New York, NY: Academic Press, Inc.

Cone, C. D. (1962). *The Theory of Induced Lift and Minimum Induced Drag of Nonplanar Lifting Systems.* Retrieved July 2011, from NASAl Technical Report Server: www.ntrs.nasa.gov

Gearboxes-Small & Miniature. (n.d.). Retrieved June 29, 2013, from Ondrives: http://ondrivesus.com/pdf/gearboxes/gearboxes-pr.pdf

Glauert, M. B. (1957). The Flow Past a Rapidly Rotating Circular Cylinder. *Proceedings of the Royal Society of London. 242*, pp. 108-115. London: The Royal Society. Retrieved March 5, 2012, from http://www.jstor.org/stable/100386

Happel, J., & Brenner, H. (1983). *Low Reynolds Number Hydrodynamics.* Boston, MA: Martinus Nijhoff Publishers.

Heiss, J. F., & Coull, J. (1952). *Chemical Engineering Progress, 48*, 133-140.

Hoerner, S. F. (1965). *Fluid-Dynamic Drag.* Bakersfield, CA: Hoerner Fluid Dynamics.

Kang, S., Choi, H., & Lee, S. (1999, November). Laminar Flow Past a Rotating Circular Cylinder. *Physics of Fluids, 11*(11), 3312-3321. doi:10.1063/1.870190

Karabelas, S. J., Koumroglou, C. D., Argyropoulos, N. C., & Markatos, N. C. (2011). High Reynolds Number Turbulent Flow Past a Rotating Cylinder. *Applied Mathematical Modelling, 36*, 379-398. doi:10.1016/j.apm.2011.07.032

Karamcheti, K. (1966). *Principles of Ideal Fluid Aerodynamics.* New York: John Wiley & Sons, Inc.

Katz, J., & Plotkin, A. (1991). *Low-Speed Aerodynamics: From Wing Theory to Panel Methods.* New York, NY: McGraw-Hill, Inc.

Kroo, I. (2000). Drag Due to Lift: Concepts for Prediction and Reduction. *Annual Review of Fluid Mechanics*, 587-617.

Lissaman, P. B. (1983). Low-Reynolds-Number Airfoils. In M. van Dyke, J. V. Wehausen, & J. L. Lumley (Eds.), *Annual Review of Fluid Mechanics* (Vol. 15, pp. 223-239). Palo Alto, CA: Annual Review Inc.

Lu, L., Qin, J.-M., Teng, B., & Li, Y.-C. (2011). Numerical Investigations of Lift Suppression by Feedback Rotary Oscillation of Circular Cylinder at Low Reynolds Number. *Physics of Fluids, 23*, 1-15. doi:10.1063/1.3560379

Lundry, J. L., & Lissaman, P. B. (1968). A Numerical Solution for the Minimum Induced Drag of Nonplanar Wings. *Journal of Aircraft, 5*(1), 17-21.

Lyapunov, S. V. (1993). Nonplanar Wings with Minimum Induced Drag. *Fluid Dynamics, 28*(2), 238-243.

Mangler, W. (1938). *The Lift Distribution of Wings with End Plates.* National Advisory Committee for Aeronautics. Springfield: National Technical Information Service.

Mittal, S. (2004). Three-Dimensional Instabilities in Flow Past a Rotating Cylinder. *Journal of Applied Mechanics, 71*, 89-95. doi:10.1115/1.1631032

Mittal, S., & Jumar, B. (2003). Flow Past a Rotating Cylinder. *Journal of Fluid Mechanics, 476*, 303-334. doi:10.1017/S0022112002002938

Moore, D. W. (1957). The Flow Past a Rapidly Rotating Circular Cylinder in a Uniform Stream. *Journal of Fluid Mechanics, 2*, 541-550.

Munk, M. M. (1921). *Minimum Induced Drag of Airfoils.* TR 121, NACA.

Ou, Y.-R. (1991). *Control of Oscillatory Forces on a Circular Cylinder by Rotation.* NASA Langley Research Center, Institute for Computer Applications in Science and Engineering. Hampton, VA: National Aeronautics and Space Administration.

Ou, Y.-R., & Burns, J. A. (1991). *Optimal Control of Lift/Drag Ratio on a Rotating Cylinder.* NASA Langley Research Center, Institute for Computer Applications in Science and Engineering. Langley, VA: National Aeronautics and Space Administration.

Padrino, J. C., & Joseph, D. D. (2006). Numerical Studye of the Steady-State Uniform Flow Past a Rotating Cylinder. *Journal of Fluid Mechanics, 557*, 191-223. doi:10.1017/S0022112006009682

Pope, A. (2009). *Basic Wing and Airfoil Theory.* Mineola, New York: Dover Publications, Inc.

Prandtl, L. (1926). *Application of the Magnus Effect to the Wind Propulsion of Ships.* Washington, D.C.: National Advisory Committee for Aeronautics.

Prandtl, L., & Tietjens, O. G. (1957). *Applied Hydro- and Aeromechanics.* New York, New York: Dover Publications, Inc.

Rae, J. W., & Pope, A. (1984). *Low-Speed Wind Tunnel Testing* (Second ed.). New York, NY: John Wiley & Sons.

Reid, E. G. (1924). *Tests of Rotating Cylinders.* Langley Memorial Aeronautical Laboratory: National Advisory Committee for Aeronautics.

Riabouchinsky, D. P. (1921). *On the Resistance of Spheres and Ellipsoids in Wind Tunnels.* Paris: National Advisory Committee for Aeronautics.

Sengupta, T. K., & Talla, S. B. (2012, March 6). Retrieved March 6, 2012, from Indian Institute of Technology Kanpur: http://home.iitk.ac.in/~tksen/TKsite/RobinsMagnus/Robins_Magnus.pdf

Stojkovic, C., Breuer, M., & Durst, F. (2002). Effect of Hidh Rotation Rates on the Laminar Flow Around a Circular Cylinder. *Physics of Fluids, 14*(9), 3160-3178. doi:10.1063/1.1492811

Stojkovic, D., Schon, P., Breuer, M., & Durst, F. (2003). On the New Vortex Shedding Mode Past a Rotating Circular Cylinder. *Physics of Fluids, 15*(5), 1257-1260. doi:10.1063/1.1562940

Taylor, J. R. (1982). *An Introduction to Error Analysis.* Mill Valley, CA: University Science Books.

The Bearing Solution. (2010). Retrieved July 27, 2013, from C-Flex Bearing Co., Inc.: http://c-flex.com/companyproducts.pdf

Thom, A. (1933). The Flow Past Circular Cylinders at Low Speeds. *Proceedings of the Royal Society of London. Series A. 141*, pp. 651-669. The Royal Society. Retrieved from http://www.jstor.org/stable/96175

Tokumaru, P. T., & Dimotakis, P. E. (1993). The Lift of a Cylinder Executing Rotary Motions in a Uniform Flow. *Journal of Fluid Mechanics, 255*, 1-10.

Tomotika, S., & Aoi, T. (1950). The Steady Flow of Viscous Fluid Past a Sphere and Circular Cylinder at Small Reynolds Numbers. *Quarterly Journal of Mechanics and Applied Mathematics, 3*(2), 140-161.

Tomotika, S., & Aoi, T. (1951). An Expansion Formula for the Drag on a Circular Cylinder Moving Through a Viscous Fluid at Small Reynolds Numbers. *Quarterly Journal of Mechanics and Applied Mathematics, 4*(4), 401-406.

Toussaint, A. (1921). *Note on the Resistance of Polished Cylinders (and Cylindrical Wires) with Generatrices Perpindicular to the Airstream.* Paris: National Advisory Committee for Aeronautics.

Tritton, D. J. (1959). Experiments on the Flow Past a Circular Cylinder at Low Reynolds Numbers. *Journal of Fluid Mechanics, 6*, 547-567.

UTSI Research Facilities. (2013). Retrieved January 8, 2013, from The University of Tennessee Space Institute: http://www.utsi.edu/research/Facilities/index.htm

Wear- and Water-Resistant Delrin® Acetal Resin. (n.d.). Retrieved May 17, 2013, from McMaster-Carr: http://www.mcmaster.com/#standard-plastic-rods/=msmbgy

White, F. M. (2006). *Viscous Fluid Flow* (Third Edition ed.). New York, NY: McGraw-Hill.

Worasinchai, S., Ingram, G., & Dominy, R. (2011, September). A Low-Reynolds-Number, High-Angle-of-Attack Investigation of Wind Turbine Aerofoils. *Proceedings of the Institution of Mechanical Engineers. Part A, Journal of Power and Energy, 226*(6), 748-763. doi:10.1177/0957650911405411

Appendix

Research in the low $10^2 \leq Re \leq 10^4$ range led to the use of a water tunnel, for which no force balance existed. Expected forces were on the magnitude of $0.1\ lbs$ up to $1.0\ lb$. In order to accommodate low forces and operation within a water tunnel, the author, with guidance from Dr. Trevor Moeller, Dr. Peter Solies, and Dr. Ahmad Vakili, designed the force balance used to collect data in for this project.

The author chose to separate all electrical devices, strain gages and associated wiring, from the water. This ruled out a typical sting type balance. Instead, a double cantilever parallelogram design was adopted, as seen in Figure A1. An upper horizontally mounted balance bar, Figure A2, upon which full wheatstone bridges were affixed was designed to measure lift moments while an identical but vertically mounted balance bar, also with full wheatstone bridges affixed, was designed to measure drag moments. A vertical and a horizontal bar, Figure A3 and Figure A4 respectively, were added to complete the parallelogram design as well as to provide a mounting location extending below the water's surface. The horizontal bar extended aft of the parallelogram portion of the balance providing the capability to manually zero moment on the lift balance bar due to high model weight by the addition of counterweights along a range of positions. C-flex frictionless bearings, Figure A5, connected the bars via balance brackets, Figure A6 and Figure A7, allowing applied forces in one axis to be translated to the appropriate balance bar, with little unintended coupling, to the other balance bar. The balance bars, and hence the complete force balance, were connected to a mounting bracket, Figure A8, that connected to a rigid rod mounted above the water tunnel. The balance bars, brackets, C-flex bearings, and hardware were stainless steel. The connecting vertical and horizontal bars were constructed from aluminum in order to reduce the system's weight.

Due to the force balance's geometry, lift was directly related to the moment, M_L, created on the lift balance bar based upon the distance between the gage location and the balance pivot, a, as given by Equation A1 and shone in Figure A1.

$$L = \frac{M_L}{a} \tag{A1}$$

For forces applied perpendicular to, but along, the vertical connecting bar, drag was directly related to the moment, M_L, created on the drag bar based upon the distance between pivots on the vertical connecting bar, b, and the distance, c, from the vertical connecting bar's lower pivot to the point of application of the force as given by Equation A2.

$$D = \frac{b}{a(b+c)} M_D \tag{A2}$$

If forces were applied perpendicular to but not along the vertical connecting bar, as was the case for this experiment due to the forward extension of the central nonrotating fuselage (CNF), drag was also a function of lift and the distance, d, by which force was separated from the axis of the vertical connecting bar as given by Equation A3.

$$D = \frac{b}{a(b+c)} M_D + \frac{d}{(b+c)} L \tag{A3}$$

The lift moment, and therefore lift, was not affected by the distance d.

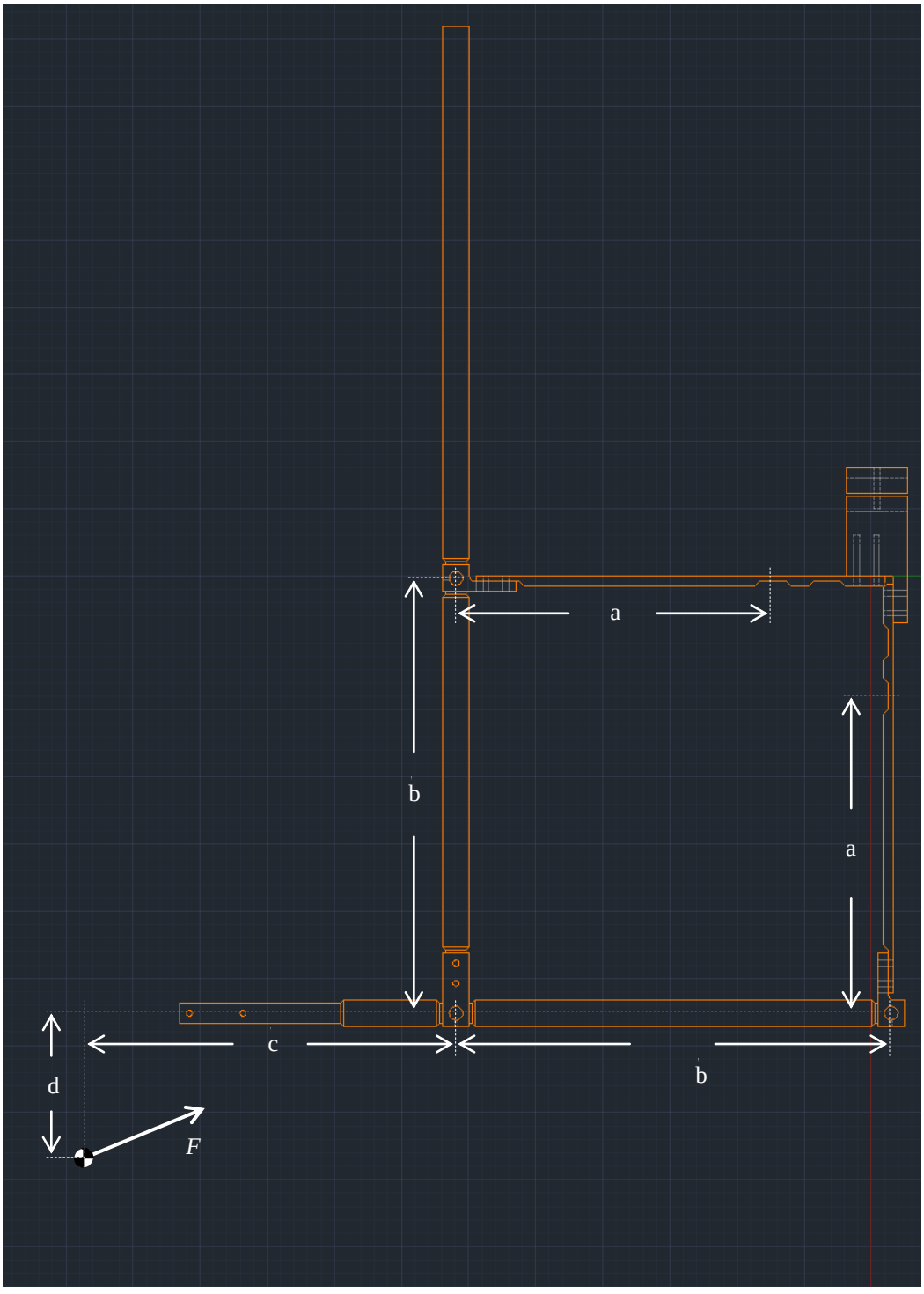

Figure A1. Complete Force Balance. Balance dimensions are presented along with a representative force *F*.

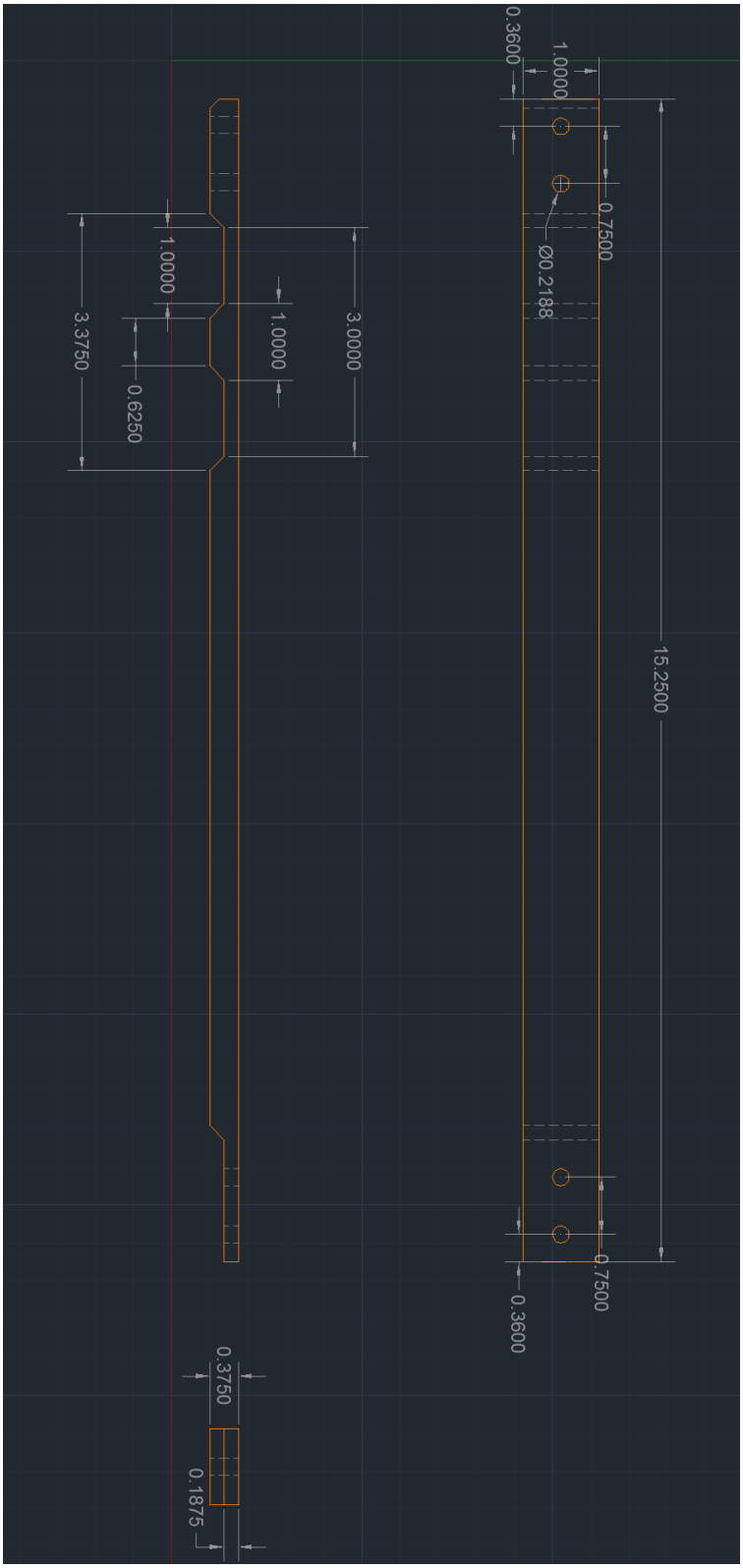

Figure A2. Balance Bar.

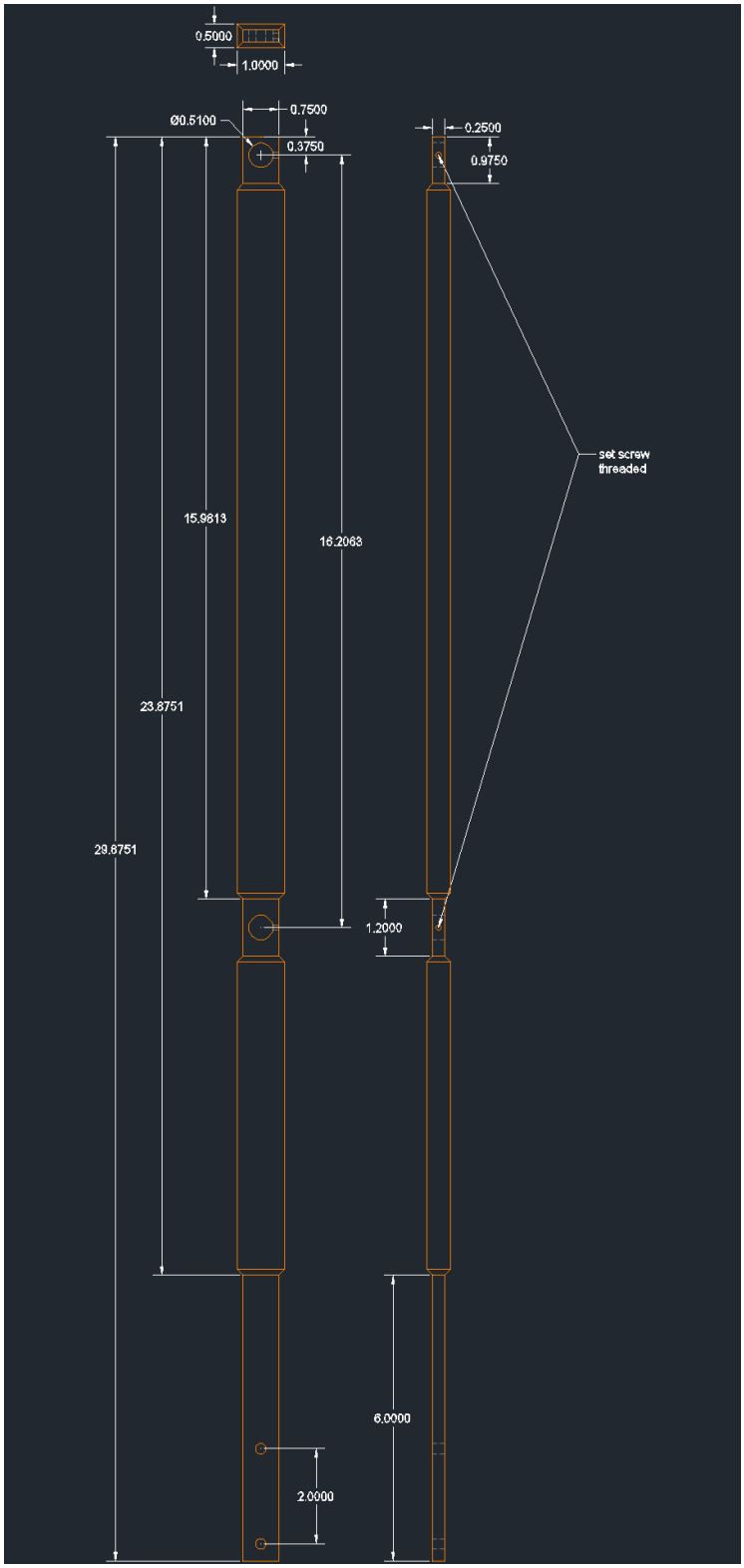

Figure A3. Vertical Connecting Bar.

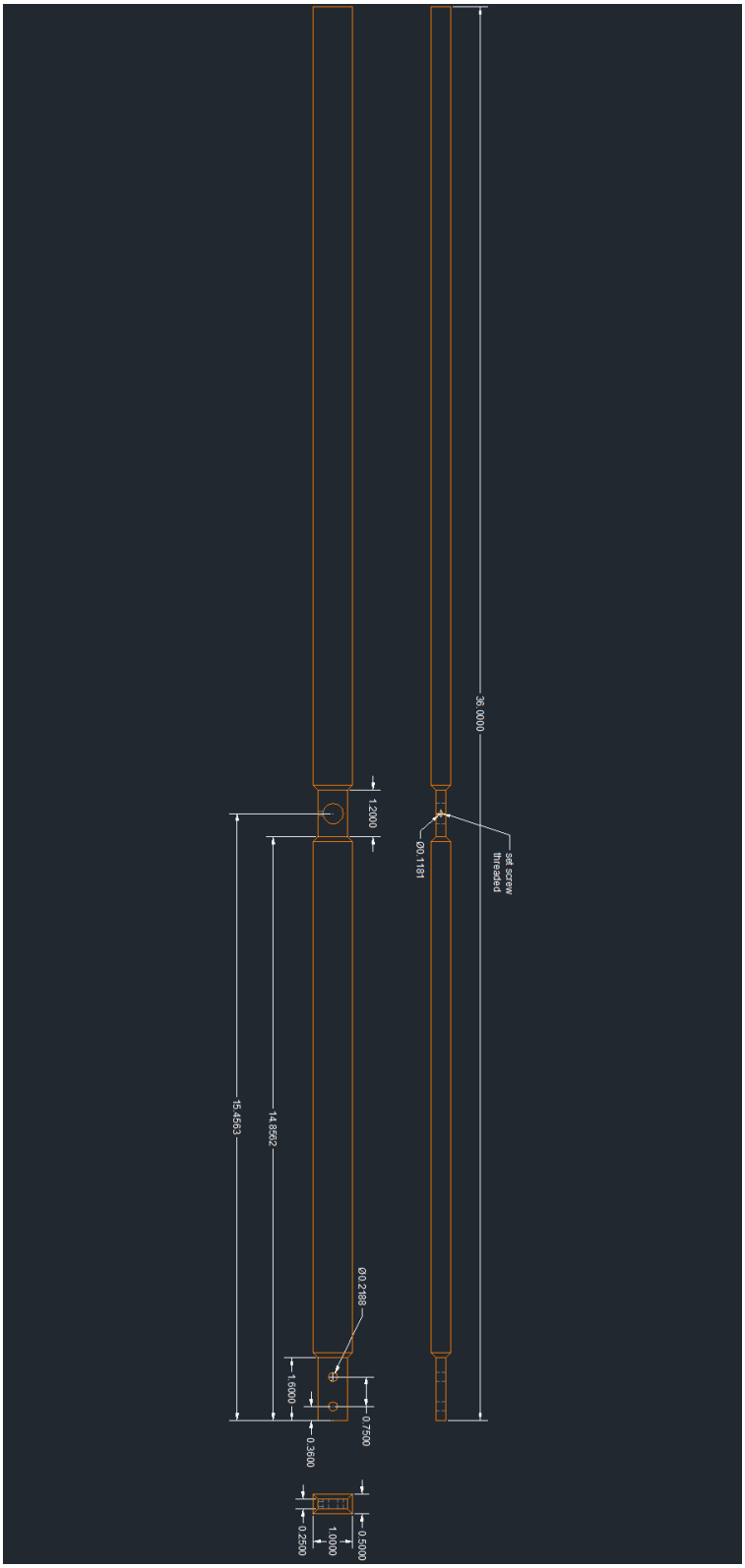

Figure A4. Horizontal Connecting Bar.

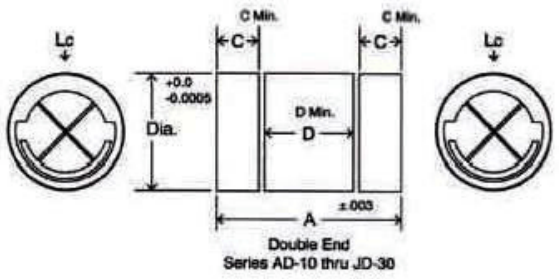

Figure A5. C-Flex Double End Frictionless Bearing. The GD-10 bearings used for the force balance were custom ordered with all load bearing surfaces of equal width, i.e $C = D$ in the figure (The Bearing Solution, 2010).

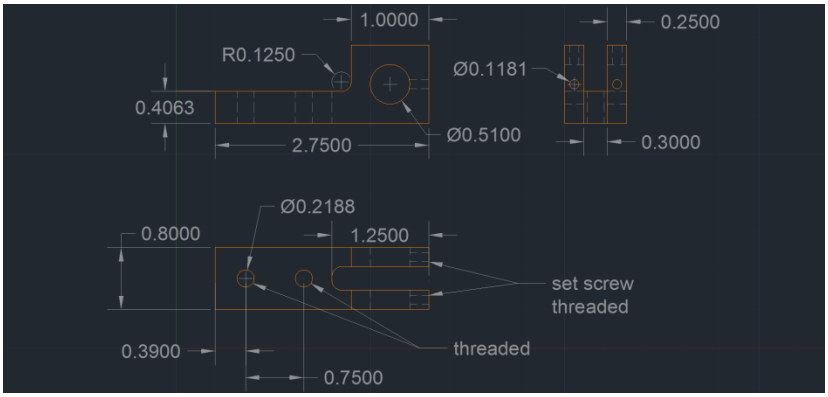

Figure A6. Balance Bar C-Flex Bracket.

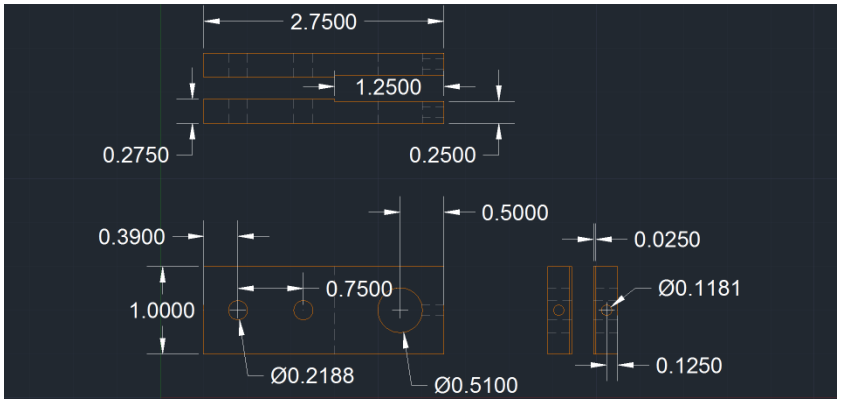

Figure A7. Vertical and Horizontal Bar C-Flex Bracket.

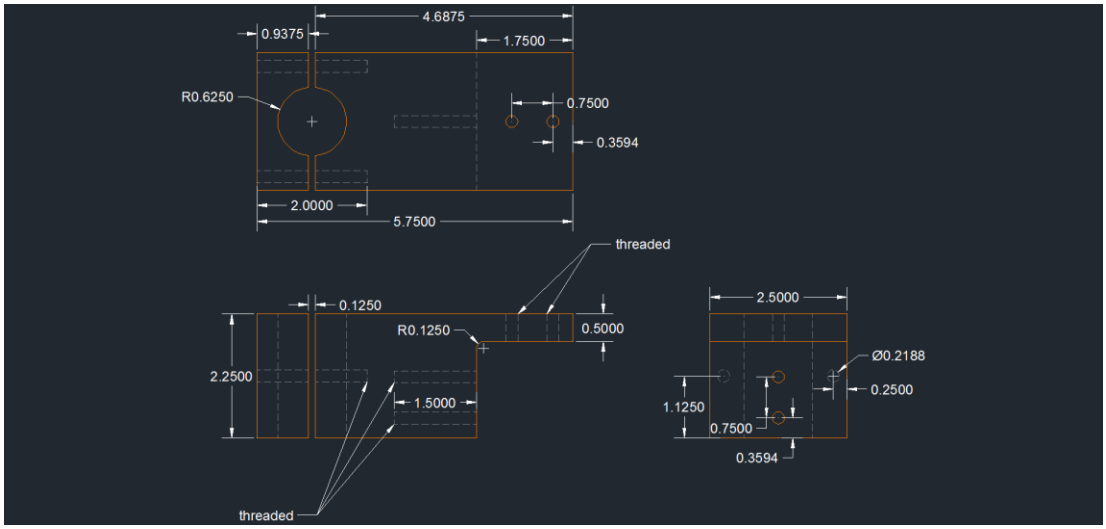

Figure A8. Force Balance Mounting Bracket.

Vita

Mark N. Callender was born in Dyersburg, TN on October 21st, 1976 to Mark and Carolyn Callender. He is the oldest of three siblings: Hannah and Sarah Brooke. He graduated from Halls High School in Halls, TN in May of 1994. He graduated with a Bachelor of Science in Aerospace Technology from Middle Tennessee State University in December of 1999. He earned a Master of Science in Aviation Systems from the University of Tennessee Space Institute in August of 2003. He worked as a Flight Test Engineer for Semcor Aerospace (later Titan Aerospace) on contract to the U.S. Army at the Aviation Technical Test Center (ATTC) in Ft. Rucker, AL during 2001. He took a faculty position in the Mathematics Department of Dyersburg State Community College (DSCC) followed by a faculty position within the Aerospace Department of Middle Tennessee State University (MTSU). He is currently an Assistant Professor in the Aerospace Department of MTSU where he coordinates the Technology Concentration and teaches courses to include Fundamentals of Aerodynamics, Aircraft Performance, and Problems in Aerospace. He married Sarah Elizabeth in June of 1998 with whom he has three childen: Elijah, Ian, and Elizabeth. He currently resides in Murfreesboro, TN.